Journal of Medicinal Chemistry

pubs.acs.org/jmc

Article

Halo and Pseudohalo Gold(I)−NHC Complexes Derived from 4,5-Diarylimidazoles with Excellent *In Vitro* and *In Vivo* Anticancer Activities Against HCC

Mianli Bian,[‖] Rong Fan,[‖] Guizhi Jiang, Yingxiang Wang, Yunlong Lu, and Wukun Liu*

Cite This: *J. Med. Chem.* 2020, 63, 9197−9211

Read Online

ACCESS | Metrics & More | Article Recommendations | Supporting Information

ABSTRACT: A series of halo and pseudohalo gold(I)−NHC complexes (NHC−Au−X) (X = Cl, Br, I, NCO, and OAc) derived from 4,5-diarylimidazoles were synthesized, structurally characterized, and analyzed for their biological activities. The most active complex was iodo(1,3-diethyl-4,5-bis(4-methoxyphenyl)imidazol-2-ylidene)gold(I) (**6**), which was at least 2-fold more cytotoxic than cisplatin and auranofin against hepatocellular carcinoma (HCC) cells. *In vivo* studies indicated that complex **6** exhibited a considerably higher anticancer efficacy (IRT = 75.7%) than cisplatin (IRT = 44.4%) in a HepG2 xenograft mouse model and ameliorated liver injury caused by CCl_4 in chronic HCC. Further studies revealed that complex **6** can inhibit the expression of the thioredoxin reductase (TrxR) both *in vitro* and *in vivo*, block the HepG2 cells in the G2/M phase, induce reactive oxygen species (ROS) production, damage mitochondrial membrane potential (MMP), and promote HepG2 cell apoptosis.

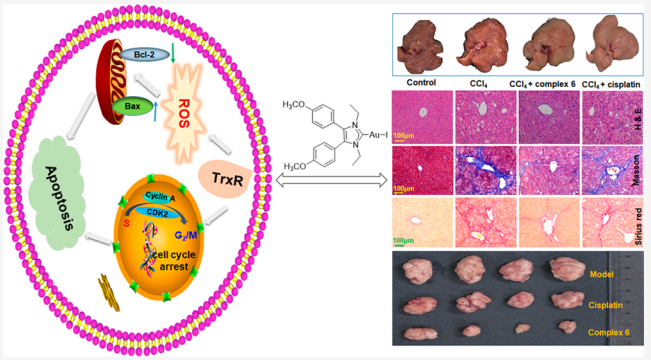

1. INTRODUCTION

Hepatocellular carcinoma (HCC), as the main malignant tumor, is recognized as the fifth most diagnosed and the second most fatal disease in the world.[1] It begins at hepatocytes and is the most common subtype of primary HCC cells.[2] Recently, the most effective treatments for HCC are surgery and liver transplantation. Even though great progress has been made in classic anti-HCC treatments, there are still many restrictions in searching for reasonable therapeutics and preventing a poor prognosis.[3,4] Hence, identifying the most effective anti-HCC treatments remain a nascent area.

Gold complexes have recently obtained increased attention because of their high anticancer activities against cancer cells, including HCC. Most of them displayed a lower toxicity, lower resistance factors, and a higher antiproliferative activity than those of platinum-based drugs.[5−9] Among gold anticancer pharmaceuticals, auranofin (an antirheumatic drug) has been or still is under clinical trials for the treatment of cancers, such as lung cancer (NCT01737502), ovarian cancer (NCT01747798), and chronic lymphocytic leukemia (NCT01419691).[6,10−12] Interestingly, recent studies reported that auranofin could inhibit HCC cell growth *in vitro* and suppress the growth of HCC tumors *in vivo* through inhibiting thioredoxin reductase (TrxR) activity.[13] Auranofin has a high potency to bind with selenocysteine residues in TrxR, owing to the formation of an irreversible and stable adduct.[8,9] TrxR is a selenoenzyme and plays an important role in redox homeostasis.[14] It can aggravate HCC growth and has been recognized as a prognostic marker and a hopeful survival indicator in HCC.[13,15−17] Thus, TrxR is a promising target and is highly demanded for HCC treatment.

However, gold complexes (e.g., auranofin) are easily metabolized by thiol-containing biomolecules, and the coordinated ligands are mostly lost before reaching the target enzyme.[5,7,8] Continuous reports have shown that sulfur-containing amino acids such as cysteine and methionine easily react with gold complexes, so the significant side effects are the generation of metal-protein adducts and resulting in nephrotoxicity.[7,9,18−21] The strong metabolization of gold complexes has limited the reasonable design of metallodrugs. Thus, the development of higher-stability gold complexes and changing their ligands have drawn wide attention.

N-Heterocyclic carbenes (NHCs) offer obvious advantages, among which are the high stability of organometallic complexes and excellent biological potentials. Many studies have confirmed that NHC carrier ligands of metal complexes,

Received: February 11, 2020
Published: August 3, 2020

https://dx.doi.org/10.1021/acs.jmedchem.0c00257
J. Med. Chem. 2020, 63, 9197−9211

Scheme 1. Synthesis of Gold(I)−NHC Complexes

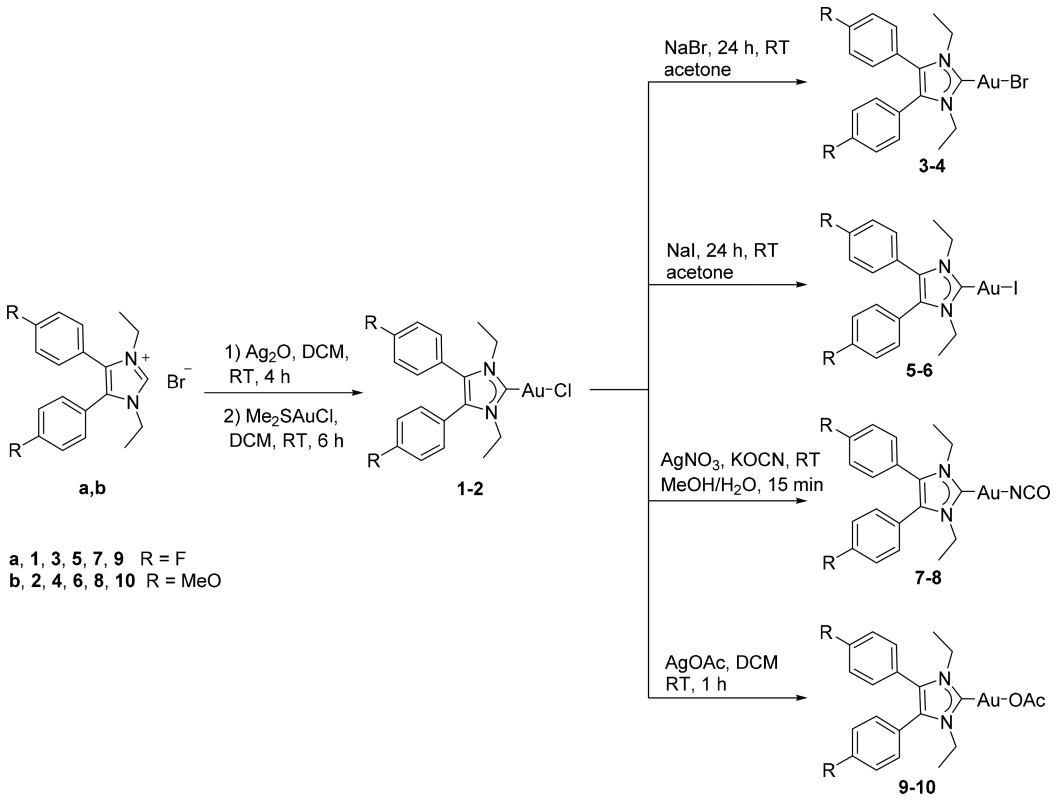

such as gold−NHC complexes, have great cytotoxic effects, showing highly modular scaffolds that are particularly adaptable to drug design.[22−29] It is relatively easy to modify the NHC substituents because the ligand backbone groups can be systematically varied, leading to complexes with differing lipophilicities or sterics.

Recently, a series of monogold(I/III)−NHC complexes derived from 4,5-diarylimidazole with effective anticancer activities were published.[22] Initial structure−activity relationship (SAR) studies demonstrated that 4-methoxy- and 4-fluoro-substituted diaryl gold(I)−NHC complexes were the most active complexes among other gold−NHC complexes. No increase in the anticancer potential was observed by oxidating the gold(I) to gold(III), exchanging the *N*-ethyl substituent, or changing the *para* position of the substituted group to the *ortho* or *meta* positions in the aromatic ring.

In the continuation of studies of this kind on monogold−NHC complexes derived from 4,5-diarylimidazole, here we report the synthesis and structural characterization of a series of halo and pseudohalo gold(I)−NHC complexes (NHC−Au−X) (X = Cl, Br, I, NCO, and OAc). We evaluated their anti-HCC activity both *in vitro* and *in vivo* and further investigated the application of an effective agent to uncover a mechanism of thioredoxin system inhibition.

2. RESULTS AND DISCUSSION

2.1. Synthesis and Characterization. The synthetic routes to halo and pseudohalo gold(I)−NHC complexes **1**−**10** are outlined in Scheme 1. 4-Methoxy- and 4-fluoro-substituted diarylimidazolium salts **a** and **b** were prepared according to our previously published methods.[23] The chloro−gold(I)−NHC complexes (**1** and **2**) were synthesized according to a previously described procedure starting from imidazolium salts **a** and **b**. They were obtained by treating imidazolium salts **a** and **b** with silver oxide in CH_2Cl_2 to form an intermediate Ag(I)−NHC complex, followed by a ligand exchange reaction with Me_2SAuCl.[22,30,31] The bromo−gold(I)−NHC complexes (**3** and **4**) and iodo−gold(I)−NHC complexes (**5** and **6**) were synthesized by treating the chloride with the corresponding sodium salts; for the synthesis of cyanato−gold(I)−NHC complexes (**7** and **8**) and acetato−gold(I)−NHC complexes (**9** and **10**), the exchange of the chloride was mediated by the appropriate silver salts. The target complexes were fully characterized by NMR spectroscopy and mass spectrometry, and their purities were tested by elemental analysis and HPLC analysis. The ^{1}H NMR spectra of gold complexes **1**−**8** are very similar and not suitable to determine their differences. However, the chemical shift of the gold-bound carbene (NCN−Au) carbon varied widely with differing halides and pseudohalides from δ 161.52 to δ 180.28 ppm in the ^{13}C NMR spectrum (Table 1).

2.2. The X-ray Crystal Analysis. To evaluate the structure of the gold(I)−NHC complexes, complex **6** was crystallized from a CH_2Cl_2/*n*-hexane solution, and the structure was determined by X-ray diffraction (Figure 1 and Tables S1−S6). The molecular structure of the iodo−gold(I)−NHC complex **6** is a linear monocarbene gold complex with common Au−

Table 1. ^{13}C NMR Chemical Shift of the Au−$C_{carbene}$ Carbon

compound	δ (ppm)	compound	δ (ppm)
1	169.68	**6**	179.24
2	168.49	**7**	167.70
3	173.27	**8**	166.54
4	172.07	**9**	164.16
5	180.28	**10**	161.52

https://dx.doi.org/10.1021/acs.jmedchem.0c00257
J. Med. Chem. 2020, 63, 9197−9211

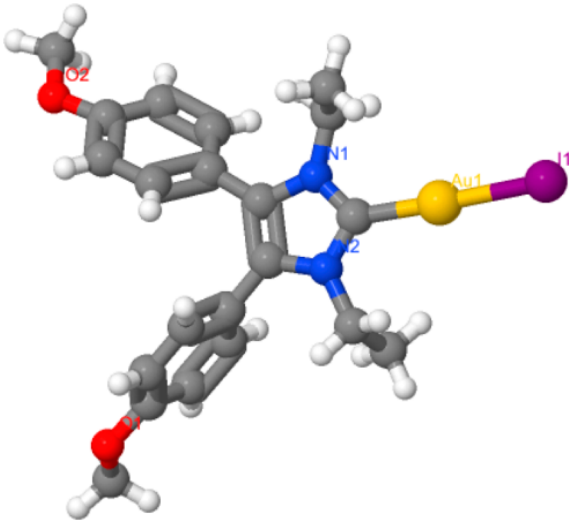

Figure 1. Crystal structure of the iodo−gold(I)−NHC complex **6**.

$C_{carbene}$ and Au−I bond lengths of 1.998(3) and 2.5524(3) Å, respectively. The C_1−Au_1−I_1 bond was almost linear with an angle of 177.99(8)°.

2.3. Stability Study. Initially, the stability of complex **6** in acetone-d_6 was tested over five days by examining the ^{1}H NMR spectra of complex **6** (Figure S1). The ^{1}H NMR spectra of complex **6** did not change significantly within five days, indicating that complex **6** was very stable in the acetone-d_6 solution. Then, the stability of complex **6** in a mixed solution (D_2O/acetone-d_6 = 1:9) was measured over time by examining the ^{1}H NMR spectra of complex **6** (Figure S2). The signals of complex **6** were stable in deuteroxide-containing acetone-d_6 solution over 4 days. Besides, we also tested the stability of complexes **2**, **4**, and **6** in a phosphate buffer solution (PBS) (pH 7.28), which contained a 100× higher concentration of GSH than that of complexes **2**, **4**, and **6** by UV−vis spectrophotometry. As shown in Figure S3, complexes **2**, **4**, and **6** were relatively stable in the PBS buffer with a high concentration of GSH. The stability of complex **6** was consistent with that of the chloro−gold(I)−NHC complex[32] and iodo(triethylphosphine)gold(I) complex.[11,33] However, it should be mentioned that some chloro−gold(I)−NHC complexes might rearrange to gold(I)−bisNHC complexes in solutions[30,34] and that iodo−gold(I)−NHC complexes might be susceptible to oxidation.[31]

2.4. *In Vitro* Antiproliferative Activity. As gold complexes displayed potential anti-HCC activity,[13] we first used the MTT assay to detect the antiproliferative activity of gold−NHC complexes **1**−**10** in HepG2, SMMC-7721, and Hep3B cancer cells. Auranofin and cisplatin were used as positive controls. As showed in Table 2, both cisplatin (HepG2, IC_{50} = 1.35 μM; SMMC-7721, IC_{50} = 3.54 μM; and Hep3B, IC_{50} = 1.15 μM) and auranofin (HepG2, IC_{50} = 1.74 μM; SMMC-7721, IC_{50} = 2.24 μM; and Hep3B, IC_{50} = 1.93 μM) were potently cytotoxic against HCC cells in the micromolar range. Among halo and pseudohalo gold(I)−NHC complexes, iodo−gold(I)−NHC complexes (**5** and **6**) and acetato−gold(I)−NHC complexes (**9** and **10**) displayed superior or comparable anti-HCC activities compared with those of cisplatin and auranofin. In particular, the most active iodo−gold(I)−NHC complex **6** (HepG2, IC_{50} = 0.50 μM; SMMC-7721, IC_{50} = 0.92 μM; and Hep3B, IC_{50} = 0.52 μM) was at least 2-fold more cytotoxic than both cisplatin and auranofin against HCC cells.

Table 2. Antiproliferative Effects Against HepG2, SMMC-7721, and Hep3B Cells After 72 h of Incubation[a]

compound	HepG2	SMMC-7721	Hep3B
cisplatin	1.35 ± 0.12	3.54 ± 0.28	1.15 ± 0.11
auranofin	1.74 ± 0.32	2.24 ± 0.24	1.93 ± 0.21
1	>20	16.14 ± 2.79	>20
2	15.50 ± 1.21	7.70 ± 0.41	7.90 ± 0.89
3	3.72 ± 0.15	9.41 ± 0.71	4.95 ± 0.11
4	4.44 ± 0.32	10.15 ± 1.29	4.71 ± 0.22
5	1.08 ± 0.12	1.88 ± 0.15	1.05 ± 0.10
6	0.50 ± 0.02	0.92 ± 0.08	0.52 ± 0.04
7	12.10 ± 1.82	8.76 ± 0.82	7.86 ± 1.22
8	3.12 ± 0.16	3.83 ± 0.18	2.41 ± 0.31
9	1.22 ± 0.11	2.47 ± 0.24	1.21 ± 0.11
10	0.71 ± 0.05	1.07 ± 0.09	0.77 ± 0.08

[a] IC_{50} values are the mean ± SD (μM).

For the halo gold(I)−NHC complexes, the size of the halogens has a large effect on the cytotoxicity of the gold complexes; a larger halogen size (I > Br > Cl) leads to a higher antiproliferative activity against HCC cells (**5** (I) > **3** (Br) > **1** (Cl) and **6** (I) > **4** (Br)> **2** (Cl)). These findings indicated that replacing the chloride (**1** and **2**) or bromide (**3** and **4**) ligand with iodide (**5** and **6**) may increase their lipophilicity, thus enhancing the drug bioavailability. For the pseudohalo gold(I)−NHC complexes, acetato−gold(I)−NHC complexes (**9** and **10**) were 3-fold more active than the corresponding cyanato−gold(I)−NHC complexes (**7** and **8**) against HCC cells. In addition, we used an XTT assay to test the cytotoxicity and calculate the IC_{50} values of the complexes as a parallel verification (Figure S4).[35] Interestingly, we observed that the results are similar to the data from the MTT assay.

The principle of the LDH assay to test the cytotoxicity is completely different from those of MTT and XTT assays.[36] LDH release is considered an important indicator of the cell membrane integrity and is extensively applied to cytotoxicity testing. Thus, we detected the LDH leakage after treatment with the complexes to cause plasma membrane disintegration. LDH release was obviously caused with the treatment of complexes **5**, **6**, **9**, and **10** (Figure S5), indicating that heavy injury and cytotoxicity to the cell membrane integrity were detected in HCC cells.

We also tested the cytotoxicity of the complexes in two different normal cells, human normal hepatocytes (LO2) and cervical epithelial (H8) cells, using the MTT assay. Interestingly, the most active complex **6** showed some degree of selectivity for HCC cells (HepG2, IC_{50} = 0.50 μM; SMMC-7721, IC_{50} = 0.92 μM; and Hep3B, IC_{50} = 0.52 μM), as it was less cytotoxic against normal cells (LO2, IC_{50} = 1.35 μM and H8, IC_{50} = 1.29 μM). Other complexes (**5**, **9**, and **10**) displayed a slight selectivity for cancer cells. Cisplatin and auranofin were less selective for HCC cells and showed similar activities against the normal cells. In addition, similar phenomena were observed in the XTT and LDH assays (Figures S6−S8).

Next, we chose reasonable doses that can injure the cancer cells but have no toxic effect on normal cells. In Figure S9, we can see that doses of 0.5, 1, and 2 μM of complex **6** could injure the HepG2 cells but have no toxic effects on LO2 cells. The doses of complex **6** caused minimally harmful effect to

https://dx.doi.org/10.1021/acs.jmedchem.0c00257
J. Med. Chem. 2020, 63, 9197−9211

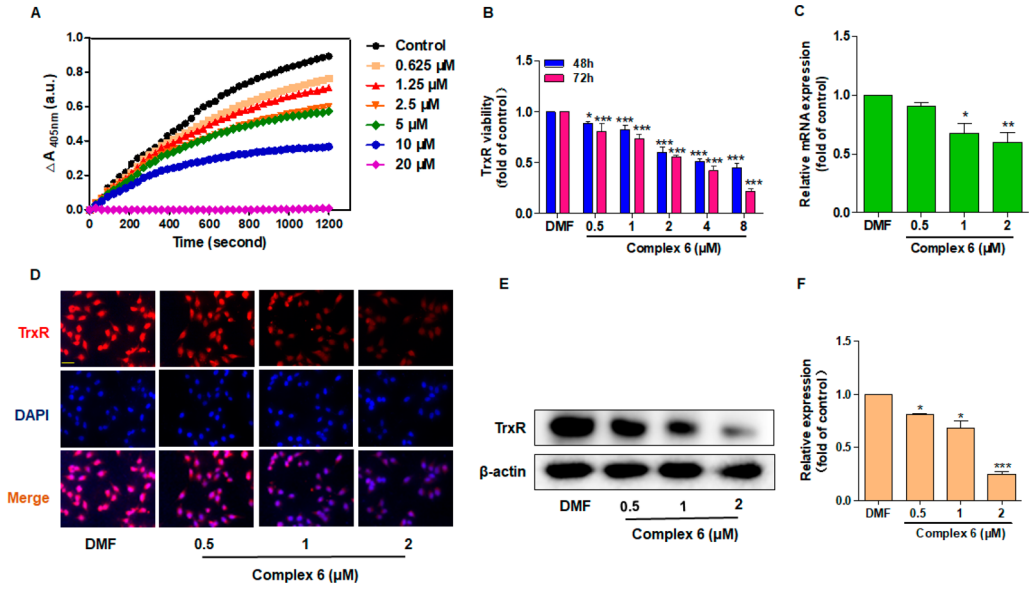

Figure 2. Complex **6** inhibited the TrxR expression. (A) Inhibition to the activity of purified TrxR by complex **6**. (B) In HepG2 cells after treatment with complex **6** for 48 and 72 h. (C) mRNA levels of TrxR. (D) Immunofluorescence analysis (original magnification is 40×). (E and F) Western blot analysis. Error bars are the SD, $n = 3$. Statistical significance of differences in mean values are $^{*}p < 0.05$, $^{**}p < 0.01$, and $^{***}p < 0.001$. Scale bars are 25 μm.

normal cells and did not show a significant difference in 24 h of treatment. In other words, these doses and complex action time are safe in cell samples.

2.5. TrxR Inhibition. TrxR is considered to be a significant target for gold complexes and is often overexpressed in HCC cells.[7,37] Thus, we tested the TrxR inhibitory activity of the most active complex **6** in both an isolated enzyme and HepG2 cells. As demonstrated in Figure 2A, the purified TrxR activity was substantially and dose-dependently inhibited by complex **6**, with an IC_{50} value of 2.14 μM. Then, we explored the TrxR inhibitory effect of complex **6** in HepG2 cells. Different concentrations of complex **6** were treated with HepG2 cells for 48 and 72 h, and TrxR assay kits were used to detect the TrxR activity. We found that complex **6** showed a TrxR inhibitory activity (IC_{50} = 2.77 μM) in 72 h of treatment (Figure 2B).

The TrxR inhibition by complex **6** in both an isolated enzyme and cells was similar to those of the reported metal-containing and natural TrxR inhibitors.[38−40] Because of the different coordination numbers, relative stabilities, and modes of structure,[41] the enzyme inhibitory activity from complex **6** was lower than that of auranofin in our previous report (IC_{50} = 82.6 nM).[42] However, it should be noted that the gold complex auranofin showed a rapid metabolization due to the conjugation to serum proteins before reaching the main target enzyme.[5−8,20]

To further evaluate the TrxR inhibition efficiency, we identified the influence of complex **6** on intracellular mRNA levels of TrxR. Real-time PCR indicated that complex **6** reduced the mRNA level in a dose-dependent manner (Figure 2C). Immunofluorescence analysis and a Western blot assay further confirmed these results (Figure 2D−F). The level of TrxR was upregulated in HepG2 cells and was decreased by complex **6** dose-dependently. Consequently, these data confirmed that complex **6** has a certain TrxR inhibitory activity *in vitro* and that TrxR may indeed be one of the main targets for this iodo−gold(I)−NHC complex.

2.6. ROS Production and Mitochondrial Dysfunction. TrxR is an important antioxidant regulator in mitochondrial dysfunction, and mitochondrial injury causes the increase of ROS.[38,43] To state this result clearly, we tested the ROS expression in HepG2 cells after complex **6** treatment for 12 h. DCFH-DA is a recognized probe and shows the burst of ROS after treatment with complex **6** (2 μM) (Figure 3A). In addition, we discussed another dye, dihydroethidium (DHE), to confirm the generation of intracellular ROS.[44] DHE can penetrate plasma membrane and intercept ROS, especially the superoxides. The ROS probe oxidizes into a red fluorescent substance in the presence of active oxygen. The red fluorescent intensity is directly proportional to the level of active oxygen in the cells. The results indicated that complex **6** could greatly trigger ROS generation (Figure 3B).

To verify whether the complex had an intrinsic luminescence that would interfere with the results of apoptosis and ROS assays, we performed fluorescence assays of complex **6**. As shown in Figure S10, there were no emission signals from 545 to 700 nm at a concentration of either 2 or 20 μM of complex **6**, while the maximum excitation wavelength of the ROS probe was 610 nm. Thus, complex **6** has no intrinsic luminescence that would interfere with the results of the apoptosis and ROS assays.

Additionally, we considered and detected other proteins related to ROS to describe the detailed mechanism of ROS more clearly. Pin1 can subject Ser/Thr−Pro phosphorylated proteins to postphosphorylation prolyl isomerization, which in turn can regulate the cell cycle and apoptosis.[45] The results by a Western blot assay indicated that complex **6** could inhibit Pin1 expression (Figure S11A and B). The NEDD8-activating enzyme (NAE) is significant among the NEDD8 conjugation pathway, which can adjust the degradation of related proteins.[46] NEDD8 is involved in important biological processes, such as cell proliferation, DNA damage repair, protein stability, transcription regulation, and chromosome formation. We found that complex **6** could obviously inhibit the NEDD8 level (Figure S11A and B). Accumulating evidence indicated that MAPKs, including ERK1/2, JNK1/2, and p38, play a critical role in intracellular ROS levels.[47−49]

https://dx.doi.org/10.1021/acs.jmedchem.0c00257
J. Med. Chem. 2020, 63, 9197−9211

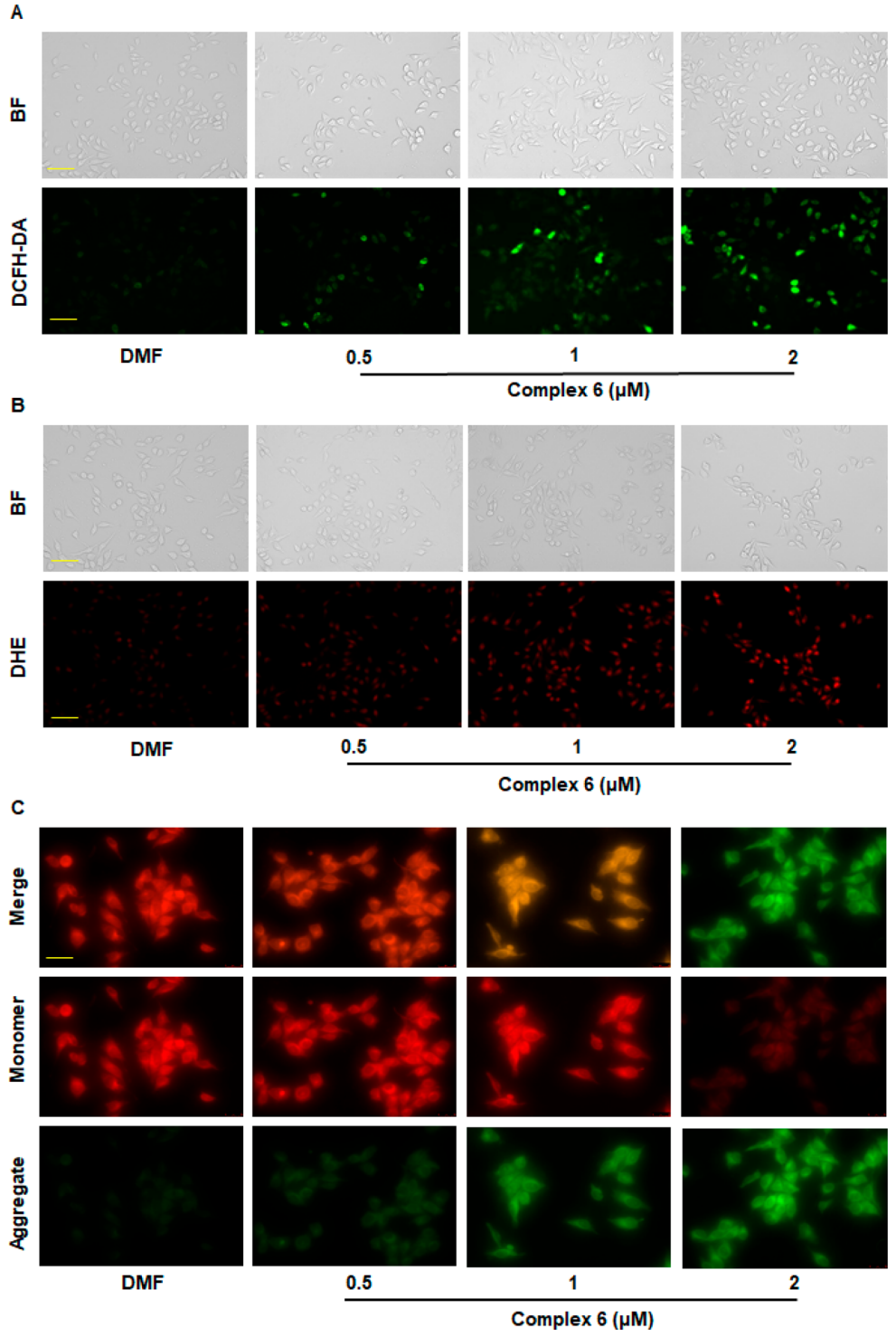

Figure 3. Complex **6** induced ROS production and mitochondrial dysfunction. (A and B) Bright field image and ROS positive cells after treatment with complex **6** by DCFH-DA and DHE assays (original magnification is 20×), respectively. (C) Mitochondrial membrane damage imaged by JC-1 staining (original magnification is 40×). Scale bars are 25 μm.

Here, the phosphorylation levels of those MAPK proteins were evaluated after 24 h of treatment with complex **6**. The levels of p-ERK1/2/ERK1/2, p-JNK1/2/JNK1/2, and p-p38/p38 increased in a concentration-dependent manner (Figure S11C and D). These results further demonstrate an enhancement of the intracellular ROS production after treatment with complex **6**.

In addition, it was reported that gold complexes could trigger antimitochondrial and apoptotic effects via inhibiting the activity of TrxR.[37] We tested the mitochondrial membrane potential (MMP) level using a JC-1 kit and observed that the green (monomeric) fluorescence increased in the complex **6** treatment group compared to the control (DMF) (Figure 3C). This result showed that the mitochondrial dysfunction may be critical in cell death processing induced by complex **6**.

https://dx.doi.org/10.1021/acs.jmedchem.0c00257
J. Med. Chem. 2020, 63, 9197−9211

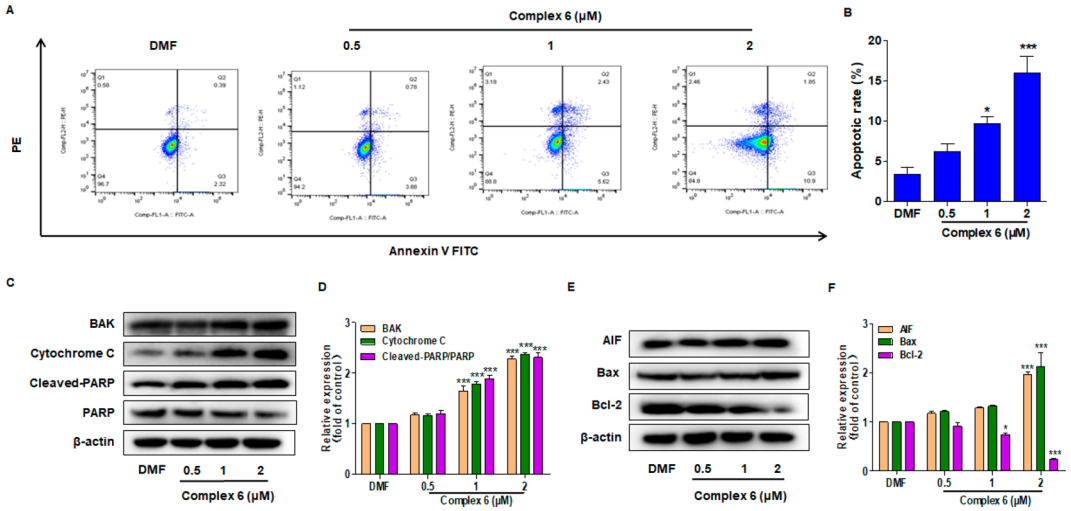

Figure 4. Complex **6** induced HepG2 cells apoptosis. (A and B) Apoptotic cells after treatment with complex **6** for 72 h. (C–F) Western blot analysis of apoptosis factors after treatment with complex **6** for 24 h. Error bars are the SD, $n = 3$. Statistical significance of differences in mean values are $^{*}p < 0.05$, $^{**}p < 0.01$, and $^{***}p < 0.001$.

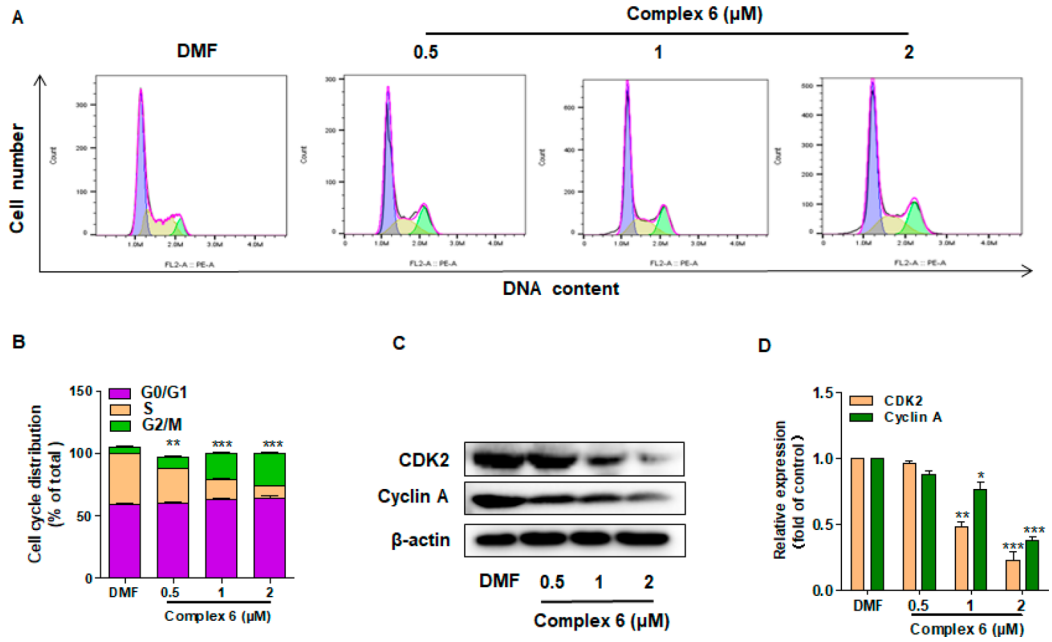

Figure 5. Cell cycle analysis. (A and B) Effects of complex **6** on cell cycle progression. (C and D) Western blot analysis. Error bars are the SD, $n = 3$. Statistical significance of differences in mean values are $^{*}p < 0.05$, $^{**}p < 0.01$, and $^{***}p < 0.001$.

Furthermore, as MMP is necessary to ATP generation, we treated HepG2 cells with complex **6** at different concentrations to verify whether complex **6** would affect ATP. Results demonstrated that the complex **6** treatment displayed a dramatically lower ATP activity than that of the DMF control (Figure S12), indicating that complex **6** could inhibit ATP release. Thus, these data demonstrated that complex **6** could impair mitochondrial function effectively in HepG2 cells and that mitochondrial dysfunction was involved in the cytotoxicity of complex **6**.

2.7. Apoptotic Pathways and Cell Cycle Analysis. ROS generation could lead to mitochondrial disorder and finally result in cell apoptosis.[50−52] After treatment with complex **6** (0.5, 1, and 2 μM) for 72 h, the apoptotic cells increased in a dose-dependent manner (Figure 4A and B). Bcl-2 can adjust the mitochondrial membrane permeabilization, and it plays a vital role in programmed cell apoptosis. To demonstrate the induction of the intrinsic pathway, we detected some important protein levels using Western blot assays. Complex **6** increased the expression of pro-apoptosis proteins (Bax, AIF, cytochrome c, and cleaved-PARP/PARP) but reduced the expression of the anti-apoptosis protein Bcl-2 (Figure 4C–F). The marker of the apoptotic factor (AIF) was tested by an immunofluorescence assay, and the result is consistent with that of the Western blot assay (Figure S13). In light of the morphological characteristics in apoptotic cells, we used Hoechst 33258 staining assays to induce the nuclear morphology with the complex **6** treatment. The cells without the complex **6** treatment demonstrated a weak blue fluorescence, appeared as regular round shapes, and also appeared brightly stained by the treatment of complex **6** (Figure S14).

https://dx.doi.org/10.1021/acs.jmedchem.0c00257
J. Med. Chem. 2020, 63, 9197−9211

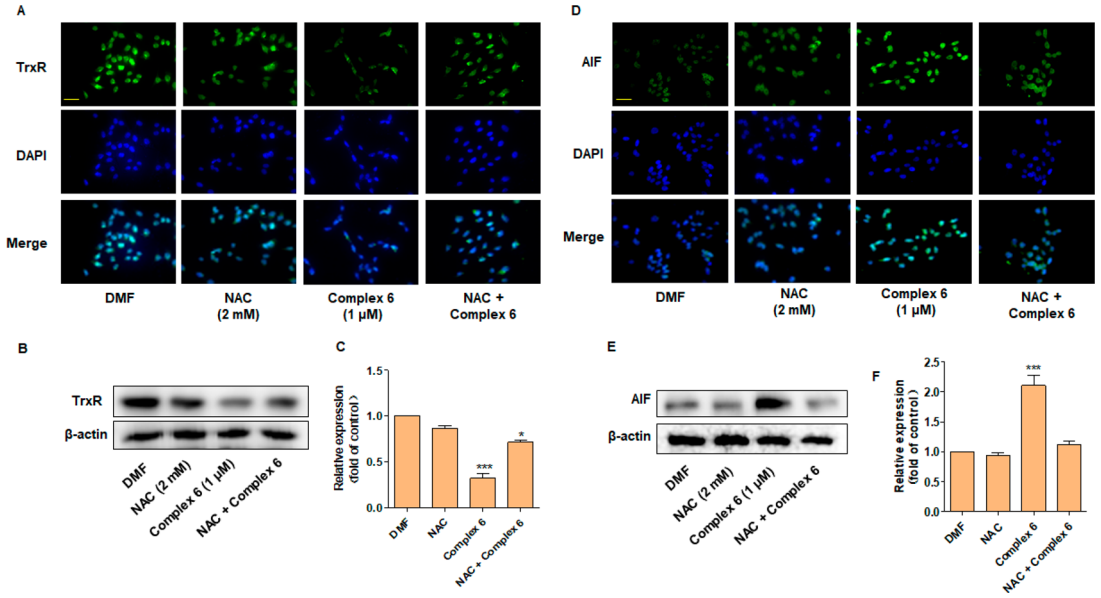

Figure 6. The activation of ROS is required for complex **6** to inhibit TrxR expression and induce HepG2 cell apoptosis. (A) Immunofluorescence analysis of TrxR in HepG2 cells treated with complex **6** and NAC at 37 °C for 24 h (original magnification is 40 ×). (B and C) Western blot assays. (D) Immunofluorescence analysis (original magnification is 40×). (E and F) Western blot analysis. Error bars are the SD, $n = 3$. Statistical significance of differences in mean values are $^{*}p < 0.05$ and $^{***}p < 0.001$. Scale bars are 25 μm.

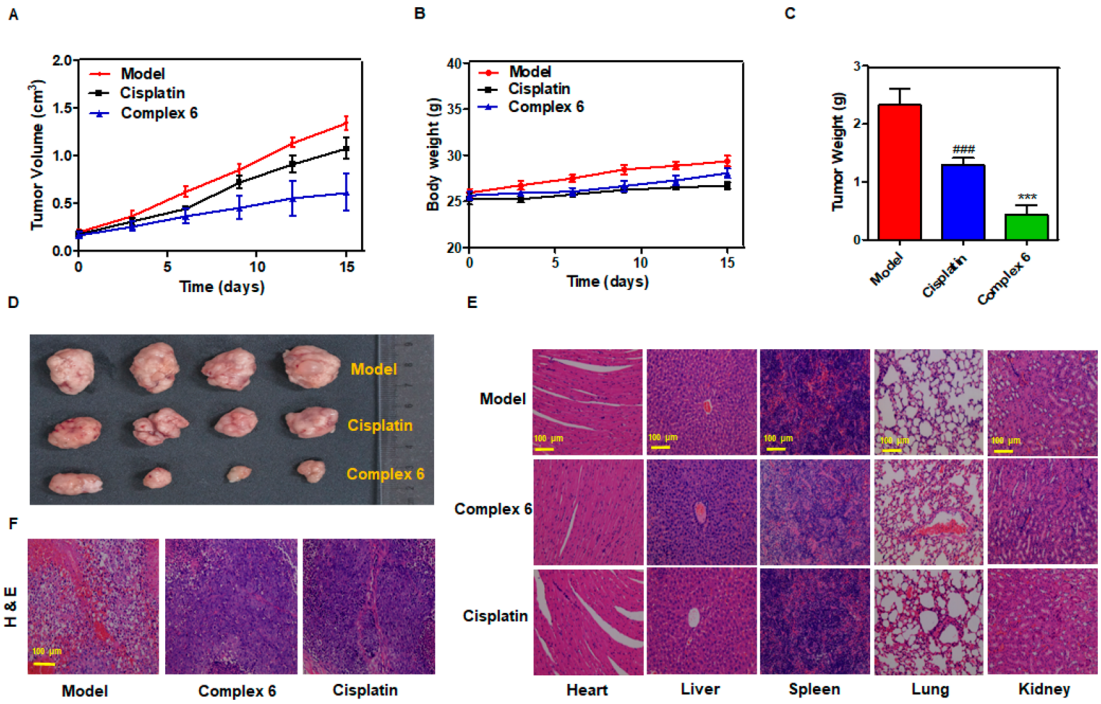

Figure 7. Complex **6** inhibited HepG2 xenograft tumor growth in nude mice. (A) The tumor volume of HepG2 xenografts in nude mice. (B) Body weight of the mice. (C) Tumor weights in nude mice. (D) Images of the representative tumors. (E and F) H&E staining of the major organs and tumor tissues (original magnification is 20×). For the statistics of each panel in this figure, data are expressed as the mean ± SD ($n = 4$); $^{###}p < 0.001$ compared with the model and $^{***}p < 0.001$ compared with cisplatin.

Next, the effect of complex **6** on cell cycle progression was detected by PI (propidium diiodide) staining. HepG2 cells were treated with complex **6** (0.5, 1, and 2 μM) for 72 h. The result indicated that the cells obviously accumulated in the G2/M phase (Figure 5A and B). Based on this, we further detected the cycle-related protein levels in the G2/M phase, and the results showed that cyclin A and CDK2 expressions were reduced in a dose-dependent manner (Figure 5C and D). Taken together, these data clearly indicated that complex **6** could induce apoptosis and cell cycle arrest in HepG2 cells.

2.8. Activating ROS is Required for Complex 6 to Depress TrxR Expression. To explore the importance of ROS-induced apoptosis for complex **6** in HepG2 cells, we used the ROS-specific scavenger *N*-acetylcysteine (NAC) (2 mM) to inhibit the ROS expression. The immunofluorescence result showed that complex **6** inhibited the TrxR level; however,

https://dx.doi.org/10.1021/acs.jmedchem.0c00257
J. Med. Chem. 2020, 63, 9197−9211

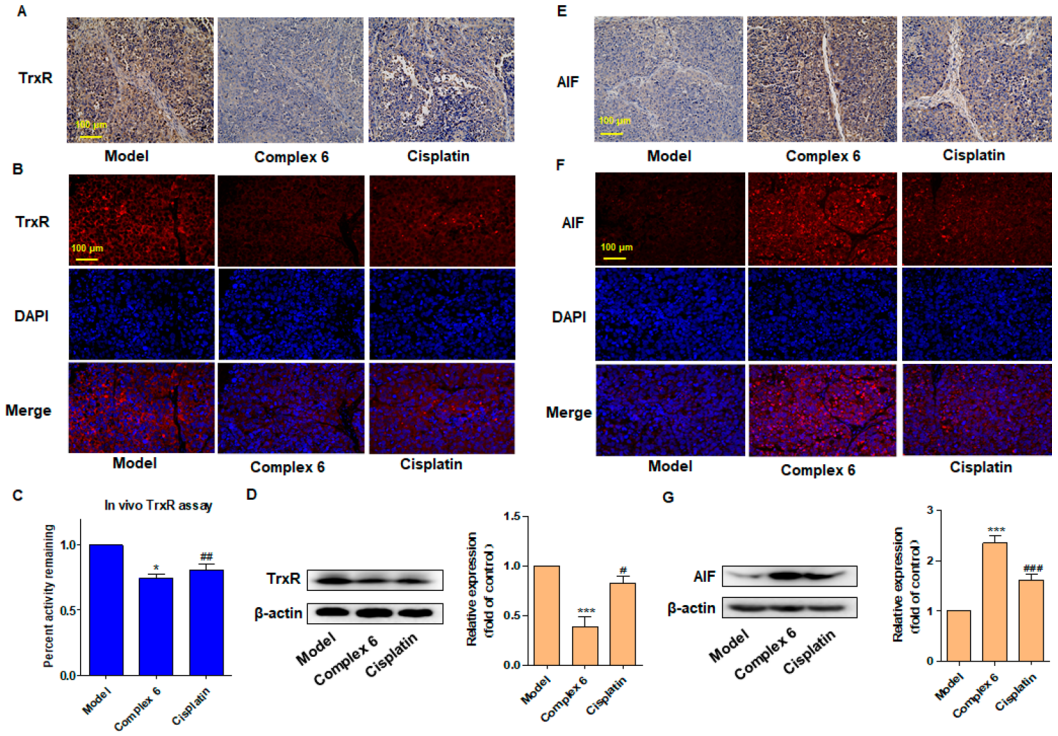

Figure 8. Complex **6** reduced TrxR activity in tumor tissues. (A and E) The expression of TrxR and AIF, respectively in tumor tissues using immunohistochemistry assays (original magnification is 20×). (B and F) Immunofluorescence assays; DAPI was used to stain the nucleus (original magnification is 40 ×). The scale bar is 100 μm. (C) TrxR activity in tumor tissues using the TrxR activity detection kit. (C, D, G, and H) Western blot assays in tumor tissue lysates. β-Actin was used as a protein loading control. For the statistics of each panel in this figure, data are expressed as the mean ± SD, $n = 4$; $^{\#}p < 0.05$, $^{\#\#}p < 0.01$, and $^{\#\#\#}p < 0.001$ compared with the model and $^{*}p < 0.05$ and $^{***}p < 0.001$ compared with cisplatin.

treatment with NAC distinctly counteracted this effect (Figure 6A). Western blot assays were consistent with the results (Figure 6B and C). Interestingly, complex **6** obviously decreased the HepG2 cell viability (Figure S15), which was partially or completely reversed by treatment with different concentrations of NAC (0.5−4 mM). These results strongly suggested both that complex **6** could activate ROS-induced apoptosis and that the biological action of complex **6** in HepG2 cells was reliant on its interaction with ROS.

AIF has both apoptosis-inducing and oxidoreductase activity. Next, the apoptotic marker (AIF) expression was tested by immunofluorescence analysis, and the result showed that the complex **6** (1 μM) treatment dramatically increased the level of AIF (Figure 6D). In addition, the result of the Western blot assay was consistent with the immunofluorescence analysis (Figure 6E and F). Collectively, these findings revealed that complex **6** could restrain the expression of TrxR and promote HepG2 cells apoptosis as well as the fact that this phenomenon can be counteracted by the NAC treatment.

During aerobic metabolism, cells perform aerobic respiration in the mitochondria. Active oxygen is a series of intermediate products of molecular oxygen in the reduction process, which can attack living macromolecular substances and cause various damages to the body. We confirmed that the complexes have significant anti-HCC cell proliferation activity under normoxic conditions. To confirm the important role of ROS in the mechanism of antiproliferative activity, we further tested the cell activity under hypoxic conditions (1% O_2, 5% CO_2, and 94% N_2 at 37 °C) for 72 h. The results using MTT, XTT, and LDH assays under hypoxic and normoxic conditions showed that our complexes had a similar inhibitory effect on tumor cell growth (Figures S16−S18). These results also fully indicated that complex **6** could inhibit the ability of TrxR to produce extensive ROS expression and finally lead to HepG2 cell apoptosis in hypoxic conditions.

2.9. *In Vivo* Antitumor Efficacy. To explore the *in vivo* impact of complex **6** against HCC, a subcutaneous xenograft model of HepG2 cells in nude mice was used. When the tumor volume reached 180−200 mm^3, these mice were randomly divided into the following three groups ($n = 4$): the model group, the cisplatin-treated (5 mg/kg) group, and the complex **6**-treated (5 mg/kg) group. Intraperitoneal administration of complex **6** for 15 days obviously reduced the HepG2 tumor volume and tumor weight vs the model and cisplatin treatment groups (Figure 7A and C). The complex **6** treatment group was well tolerated and without clear weight loss compared to the model and cisplatin treatment groups (Figure 7B). In addition, the complex **6**-treated group showed an inhibition rate of tumor growth (IRT) as high as 75.7%, significantly higher than those of cisplatin (IRT = 44.4%) (Figure 7C and D) and the rhodium(I)−NHC complex (IRT = 45%, 10 mg/kg) with a similar scaffold.[50] The tumor nucleus in the model group was heteromorphic, displaying focal necrosis, pathological mitosis, and many new vessels in the tumor tissues. This phenomenon was alleviated by the complex **6** treatment, showing better effects than cisplatin treatment at the same dose (Figure 7F). In addition, H&E staining analysis of the complex **6**-treated group further showed its nontoxicity in mouse hearts, livers, spleens, lungs, and kidneys compared with the model group and the cisplatin-treated group (Figure 7E). Thus, we can conclude that complex **6** can remarkably inhibit HCC tumor growth while simultaneously not damaging the hepatocellular morphology and increasing necrotic hepatocytes.

https://dx.doi.org/10.1021/acs.jmedchem.0c00257
J. Med. Chem. 2020, 63, 9197−9211

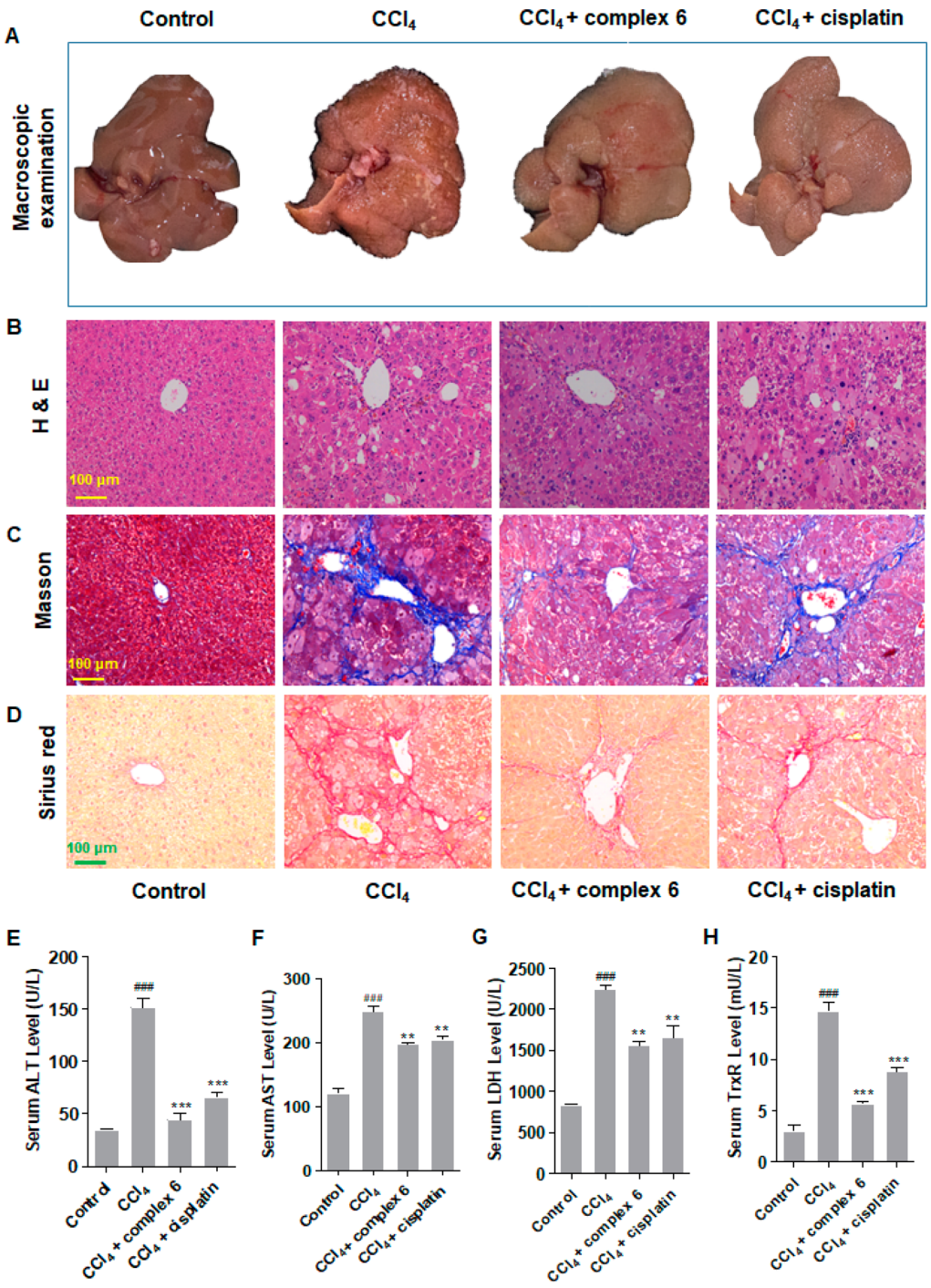

Figure 9. Complex **6** reduced the accumulation of collagen and ameliorated the damage of liver tissues *in vivo*. (A) The liver morphological changes. (B) H&E staining in liver tissues. (C and D) Masson and Sirius red staining. (E−H) Determination of serum ALT, AST, LDH, and TrxR levels, respectively. The original magnification is20×. For the statistics of each panel in this figure, data are expressed as the mean ± SD, $n = 5$; $^{###}p < 0.001$ compared with the control and $^{*}p < 0.05$, $^{**}p < 0.01$, and $^{***}p < 0.001$ compared with the CCl_4 group.

Furthermore, TrxR levels in tumor tissues were measured by the immunohistochemistry and TrxR kit assays. Results indicated that the complex **6** treatment group obviously reduced the TrxR activity compared to the cisplatin treatment group (Figure 8A and C). Immunofluorescence and Western blot analyses of the three groups were consistent with the immunohistochemistry assay results (Figure 8B and D). In addition, we detected the expression of the apoptosis marker AIF; the results indicated that the complex **6**-treated group could increase the levels of AIF compared to the model group and the cisplatin-treated group, indicating that complex **6** induced apoptosis in tumor tissues (Figure 8E−G). Taken together, treatment with complex **6** could inhibit the tumor growth *in vivo* by depressing the TrxR expression and have a better effect than the treatment with cisplatin.

2.10. Complex 6 Ameliorates Liver Injury and the Tumor Microenvironment *In Vivo*. The animal models of HCC have supplied related information about the pathogenesis and molecular mechanisms.[4,50,53] Intraperitoneal injection of carbon tetrachloride (CCl_4) is a very mature

https://dx.doi.org/10.1021/acs.jmedchem.0c00257
J. Med. Chem. 2020, 63, 9197−9211

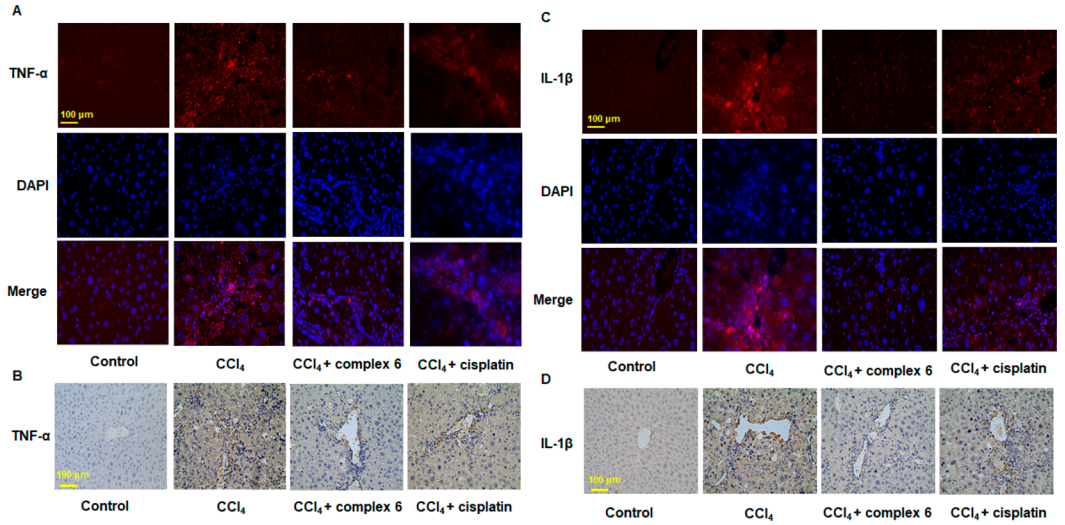

Figure 10. Complex **6** ameliorated the inflammatory reaction to relieve liver injury. (A and C) Liver tissues were stained with immunofluorescence using antibodies against TNF-α and IL-1β. DAPI was used to stain the nucleus. The original magnification is 40 ×. (B and D) Immunohistochemistry staining. The original magnification is 20 ×.

method to cause liver injury.[54] To further assess the *in vivo* anticancer activities of complex **6** against HCC, we chose continuous intraperitoneal injection of CCl_4 (5 mL/kg) into the ICR mice for 16 weeks and then treatment with complex **6** (5 mg/kg) and a positive control (cisplatin, 5 mg/kg) to study the therapeutic potential of complex **6** in regard to liver damage.

All mice livers treated with CCl_4 displayed cirrhotic features with rough and darkened surfaces (Figure 9A). H&E staining analysis indicated that the complex **6** treatment group (5 mg/kg) had remarkably improved morphological changes compared to those of the cisplatin treatment group (5 mg/kg) and CCl_4 model group (Figure 9B). The generation of collagen accompanies fibrogenesis; therefore, we used Masson staining and Sirius red staining to test and verify the collagen accumulation. The results indicated that the collagen was significantly increased in the CCl_4-injured liver; interestingly, it was obviously decreased in the complex **6** treatment group (Figure 9C and D). In addition, the levels of the liver injury markers (alanine aminotransferase (ALT), aspartate aminotransferase (AST), and LDH) were effectively reversed in the complex **6** treatment group (Figure 9E−G). Based on the results of the liver injury, ELASA analyses further confirmed that the level of TrxR in serum was high in the CCl_4-injured liver, which is consistent with the report that the TrxR levels in serum were recently identified as possible prognostic markers for HCC.[17] As expected, treatment with complex **6** dramatically reversed these changes (Figure 9H). In general, these data powerfully demonstrated that treatment with complex **6**, which showed better activity in these assays than treatment with cisplatin, did decrease the collagen accumulation and improve the liver injury in HCC model mice.

Chronic liver injury is usually accompanied by the generation of inflammation.[55] Inflammatory cells and regulatory factors exist in most liver injury microenvironments.[56] Inflammation is involved in tumor angiogenesis and tumor cell growth. Besides, the angiogenesis is first triggered by the inflammatory factor interleukin-1β (IL-1β).[57] As the results showed, serious inflammatory cell infiltration in CCl_4 model livers was depressed after the complex **6** treatment, as characterized by a decrease in the number of tumor necrosis factor (TNF-α) and IL-1β using immunohistochemistry and immunofluorescence analyses (Figure 10A−D). It should be noted that cisplatin was slightly less active than complex **6** against HCC in these assays. In short, these results also indicated that treatment with complex **6** could ameliorate the CCl_4-induced liver injury *in vivo* by reducing the TrxR expression and inflammation level.

3. CONCLUSIONS

A series of halo and pseudohalo gold(I)−NHC complexes were prepared, structurally characterized, and biologically investigated. A preliminary SAR study demonstrated that iodo−gold(I)−NHC complex **6** represented an effective cytostatic with cytotoxic effects against HCC (HepG2, SMMC-7721, and Hep3B) cells up to 3-fold higher than cisplatin or auranofin. This complex could inhibit the expression of TrxR, block HepG2 cells in the G2/M phase, induce the accumulation of ROS, damage the MMP, and promote HepG2 cell apoptosis.

In vivo studies demonstrated that complex **6** obviously decreased tumor growth and had a controllable toxicity. It repressed collagen accumulation and improved the liver injury in a chronic HCC model. Further studies also confirmed that this complex could inhibit HepG2 xenograft tumor growth in nude mice and ameliorate liver injury by inhibiting TrxR expression and the inflammation level, showing better effects than those of cisplatin. Overall, these *in vitro* and *in vivo* results suggest that complex **6** may significantly induce HCC cell death through enhanced oxidative stress and can be considered as a promising potential therapeutic candidate for the treatment of HCC.

4. EXPERIMENTAL SECTION

4.1. Materials and Methods. The materials for synthesis were purchased from Energy Chemical and used without further purification. All deuterated solvents were bought from Cambridge Isotope Lab, Inc. (CIL). Antibodies, such as cleaved-PARP, BAK and cytochrome c for Western blot, were purchased from Abcam. p-ERK, p-JNK, and p-p38 were purchased from Affinity Biosciences. ERK, JNK, and p38 were purchased from Wanlei Bio. Pin1 and NEDD8 were acquired from Proteintech. The JC-1 kit, the ROS assay kit, and

https://dx.doi.org/10.1021/acs.jmedchem.0c00257
J. Med. Chem. 2020, 63, 9197−9211

the ATP assay kit were purchased from Beyotime Biotechnology. Purified rat liver TrxR was purchased from Sigma Aldrich. The TrxR activity detection kit was bought from Solarbio. The purities of the newly synthesized gold−NHC complexes (>95%) were verified by elemental analyses and HPLC analysis (Figure S20).

^{1}H NMR and ^{13}C NMR spectra were recorded on a Bruker Avance III HD 500 MHz spectrometer. The $(CH_3)_4Si$ signal was used as a reference. The purities of gold−NHC complexes were detected at the instrumental analysis center of China Pharmaceutical University and obtained on a PE 2400 Series II instrument. HPLC analysis was performed on a Waters ACQUITY Arc system equipped with a 2998 PDA detector. UV−vis spectra were recorded on a Shimadzu UV2400 spectrophotometer. The MALDI-TOF/TOF mass spectrometer used was a Bruker Daltonics ultrafl extreme MALDI TOF/TOF instrument. X-ray single crystal diffractometry measurements was recorded by a BRUKER Smart APEX II CCD instrument. The flow cytometer used in the cell cycle and apoptosis experiments was a BD C6 Plus instrument. The fluorescence spectra were detected by a Hitachi fluorescence spectrophotometer, model F-7000.

4.2. Synthesis and Characterization. *4.2.1. The Synthesis of Chloro−Gold(I)−NHC complexes **1** and **2**.* A mixture of imidazolium salts **a** (786.4 mg, 2 mmol) or **b** (834.7 mg, 2 mmol) and silver oxide (278.1 mg, 1.2 mmol) in CH_2Cl_2 (20 mL) was stirred overnight under a N_2 atmosphere. Then, $(Me_2S)AuCl$ (589.1 mg, 2 mmol) was added, and the mixture was kept in the same conditions to continue the reaction for 6 h. The reaction mixture was filtered through Celite, and the filtrate was condensed *in vacuo* to acquire the crude product. The crude product was further purified by a chromatography column and recrystallized from CH_2Cl_2/*n*-hexane to yield a white solid.

*4.2.2. Chloro(1,3-diethyl-4,5-bis(4-fluorophenyl)imidazol-2-ylidene)gold(I) (**1**).* Yield 84%. ^{1}H NMR (500 MHz, $CDCl_3$, 20 °C): δ 7.16 (dd, J = 8.7, 5.2 Hz, 4H, ArH), 7.05 (t, J = 8.5 Hz, 4H, ArH), 4.15 (q, J = 7.2 Hz, 4H, $NC\underline{H}_2CH_3$), 1.28 (t, J = 7.2 Hz, 6H, $NCH_2C\underline{H}_3$). ^{13}C NMR (126 MHz, $CDCl_3$, 20 °C): δ 169.68 (N$\underline{C}$N−Au), 164.18, 162.19, 132.42, 132.35, 123.49, 123.46, 116.40, 116.22 (ArC), 130.34 (N$\underline{C}$=$\underline{C}$N), 44.44 (NCH_2CH_3), 16.90 (NCH_2CH_3). MALDI-TOF/TOF-MS: 544.228 $[M]^+$, 567.077 $[M + Na]^+$, 583.050 $[M + K]^+$. Anal. Calcd for $C_{19}H_{18}AuClF_2N_2$: C, 41.89; H, 3.33; N, 5.14. Found: C, 41.81; H, 3.14; N, 4.99.

*4.2.3. Chloro(1,3-diethyl-4,5-bis(4-methoxyphenyl)imidazol-2-ylidene)gold(I) (**2**).* Yield 53%. ^{1}H NMR (500 MHz, $CDCl_3$, 20 °C): δ 7.11 (d, J = 8.5 Hz, 4H, ArH), 6.87 (d, J = 8.6 Hz, 4H, ArH), 4.16 (q, J = 7.1 Hz, 4H, $NC\underline{H}_2CH_3$), 3.80 (s, 6H, $ArOC\underline{H}_3$), 1.30 (t, J = 7.2 Hz, 6H, $NCH_2C\underline{H}_3$). ^{13}C NMR (126 MHz, $CDCl_3$, 20 °C): δ 168.55 (N$\underline{C}$N−Au), 160.14, 131.80, 119.87, 114.30 (ArC), 130.76 (N$\underline{C}$=$\underline{C}$N), 55.27 ($ArO\underline{C}H_3$), 44.25 ($N\underline{C}H_2CH_3$), 16.93 ($NCH_2\underline{C}H_3$). MALDI-TOF/TOF-MS: 568.104 $[M]^+$, 533.172 $[M - Cl]^+$, 591.133 $[M + Na]^+$. Anal. Calcd for $C_{21}H_{24}AuClN_2O_2$: C, 44.34; H, 4.25; N, 4.92. Found: C, 44.03; H, 4.02; N, 4.74.

*4.2.4. The Synthesis of Gold(I)−NHC complexes **3**−**6**.* **1** (60 mg, 0.11 mmol) and sodium bromide (45.3 mg, 0.44 mmol) or potassium iodide (73.1 mg, 0.44 mmol) were dissolved in 2 mL of anhydrous acetone, and the mixture was stirred under N_2 for 24 h to form **3** or **5**, respectively. Meanwhile, **2** (60 mg, 0.105 mmol) and sodium bromide (43.4 mg, 0.42 mmol) or potassium iodide (70 mg, 0.42 mmol) were dissolved in 2 mL of anhydrous acetone, and the mixture was stirred under N_2 for 24 h to form **4** or **6**, respectively. After the solvent was removed *in vacuo*, the residue was dissolved in CH_2Cl_2 and then filtered over a bed of Celite. The filtrate was carefully evaporated to dryness under reduced pressure to yield a colorless solid, which was further purified through a plug of silica.

*4.2.5. Bromo(1,3-diethyl-4,5-bis(4-fluorophenyl)imidazol-2-ylidene)gold(I) (**3**).* Yield 59%. ^{1}H NMR (500 MHz, $CDCl_3$, 20 °C): δ 7.23−7.18 (m, 4H, ArH), 7.12−7.07 (m, 4H, ArH), 4.20 (q, J = 7.2 Hz, 4H, $NC\underline{H}_2CH_3$), 1.33 (t, J = 7.2 Hz, 6H, $NCH_2C\underline{H}_3$). ^{13}C NMR (126 MHz, $CDCl_3$, 20 °C): δ 173.28 (N$\underline{C}$N−Au), 164.18, 162.16, 132.41, 132.34, 123.49, 123.47, 116.40, 116.23 (ArC), 130.27 (N$\underline{C}$=$\underline{C}$N), 44.33 ($N\underline{C}H_2CH_3$), 16.90 ($NCH_2\underline{C}H_3$).

*4.2.6. Bromo(1,3-diethyl-4,5-bis(4-methoxyphenyl)imidazol-2-ylidene)gold(I) (**4**).* Yield 63%. ^{1}H NMR (500 MHz, $CDCl_3$, 20 °C): δ 7.11 (d, J = 8.7 Hz, 4H, ArH), 6.87 (d, J = 8.7 Hz, 4H, ArH), 4.16 (q, J = 7.2 Hz, 4H, $NC\underline{H}_2CH_3$), 3.80 (s, 6H, $ArOC\underline{H}_3$), 1.30 (t, J = 7.2 Hz, 6H, $NCH_2C\underline{H}_3$). ^{13}C NMR (126 MHz, $CDCl_3$, 20 °C): δ 172.07 (N$\underline{C}$N−Au), 160.11, 131.78, 119.86, 114.28 (ArC), 130.68 (N$\underline{C}$=$\underline{C}$N), 55.26 ($ArO\underline{C}H_3$), 44.15 ($N\underline{C}H_2CH_3$), 16.94 ($NCH_2\underline{C}H_3$).

*4.2.7. Iodo(1,3-diethyl-4,5-bis(4-fluorophenyl)imidazol-2-ylidene)gold(I) (**5**).* Yield 48.3%. ^{1}H NMR (500 MHz, $CDCl_3$, 20 °C): δ 7.19 (dd, J = 8.5, 5.3 Hz, 4H, ArH), 7.08 (t, J = 8.5 Hz, 4H, ArH), 4.19 (q, J = 7.2 Hz, 4H, $NC\underline{H}_2CH_3$), 1.32 (t, J = 7.2 Hz, 6H, $NCH_2C\underline{H}_3$). ^{13}C NMR (126 MHz, $CDCl_3$, 20 °C): δ 180.29 (N$\underline{C}$N−Au), 164.16, 162.16, 132.41, 132.35, 123.51, 123.48, 116.39, 116.22 (ArC), 130.17 (N$\underline{C}$=$\underline{C}$N), 44.08 ($N\underline{C}H_2CH_3$), 16.94 ($NCH_2\underline{C}H_3$). MALDI-TOF/TOF-MS: 509.137 $[M - I]^+$. Anal. Calcd for $C_{19}H_{18}AuF_2IN_2$: C, 35.87; H, 2.85; N, 4.40. Found: C, 35.96; H, 2.65; N, 4.28.

*4.2.8. Iodo(1,3-diethyl-4,5-bis(4-methoxyphenyl)imidazol-2-ylidene)gold(I) (**6**).* Yield 58%. ^{1}H NMR (500 MHz, $CDCl_3$, 20 °C): δ 7.13 (d, J = 8.7 Hz, 4H, ArH), 6.88 (d, J = 8.7 Hz, 4H, ArH), 4.18 (q, J = 7.2 Hz, 4H, $NC\underline{H}_2CH_3$), 3.81 (s, 6H, $ArOC\underline{H}_3$), 1.33 (t, J = 7.2 Hz, 6H, $NCH_2C\underline{H}_3$). ^{13}C NMR (126 MHz, $CDCl_3$, 20 °C): δ 179.24 (N$\underline{C}$N−Au), 160.10, 131.77, 119.87, 114.29 (ArC), 130.56 (N$\underline{C}$=$\underline{C}$N), 55.27 ($ArO\underline{C}H_3$), 43.90 ($N\underline{C}H_2CH_3$), 16.97 ($NCH_2\underline{C}H_3$). MALDI-TOF/TOF-MS: 533.180 $[M - I]^+$, 679.549 $[M + H_3O]^+$. Anal. Calcd for $C_{21}H_{24}AuClN_2O_2$: C, 44.34; H, 4.25; N, 4.92. Found: C, 44.03; H, 4.02; N, 4.74.

*4.2.9. The Synthesis of Cyanato−Gold(I)−NHC Complexes **7** and **8**.* Silver nitrate (31.1 mg, 0.183 mmol) was dissolved in a mixture solution comprised of 0.3 mL of CH_3OH and 0.1 mL of H_2O and then slowly added to a mixture (3 mL of CH_3OH/0.6 mL of H_2O) with potassium cyanate (35.7 mg, 0.44 mmol) and **1** (60 mg, 0.11 mmol) or **2** (62.7 mg, 0.11 mmol), which immediately gave a white precipitate. The reaction mixture was stirred for 15 min and then filtered, and the filtrate was carefully evaporated *in vacuo*. The residue was recrystallized from CH_2Cl_2/*n*-hexanes to yield a white solid.

*4.2.10. Cyanato(1,3-diethyl-4,5-bis(4-fluorophenyl)imidazol-2-ylidene)gold(I) (**7**).* Yield 49%. ^{1}H NMR (500 MHz, $CDCl_3$, 20 °C): δ 7.19 (dd, J = 8.5, 5.3 Hz, 4H, ArH), 7.07 (t, J = 8.5 Hz, 4H, ArH), 4.15 (q, J = 7.2 Hz, 4H, $NC\underline{H}_2CH_3$), 1.32 (t, J = 7.2 Hz, 6H, $NCH_2C\underline{H}_3$). ^{13}C NMR (126 MHz, $CDCl_3$, 20 °C): δ 167.71 (N$\underline{C}$N−Au), 164.20, 162.20, 132.47, 132.40, 123.49, 123.46, 116.38, 116.21 (ArC), 130.47 (N$\underline{C}$=$\underline{C}$N), 129.43 (N$\underline{C}$O), 44.46 ($N\underline{C}H_2CH_3$), 16.91 ($NCH_2\underline{C}H_3$). MALDI-TOF/TOF-MS: 509.129 $[M - NCO]^+$, 526.157 $[M - CNO + OH]^+$. Anal. Calcd for $C_{20}H_{18}AuF_2N_3O$: C, 43.57; H, 3.29; N, 7.62. Found: C, 43.52; H, 3.33; N, 7.21.

*4.2.11. Cyanato(1,3-diethyl-4,5-bis(4-methoxyphenyl)imidazol-2-ylidene)gold(I) (**8**).* Yield 43%. ^{1}H NMR (500 MHz, $CDCl_3$, 20 °C): δ 7.10 (d, J = 8.5 Hz, 4H, ArH), 6.87 (d, J = 8.6 Hz, 4H, ArH), 4.13 (q, J = 7.2 Hz, 4H, $NC\underline{H}_2CH_3$), 3.80 (s, 6H, $ArOC\underline{H}_3$), 1.30 (t, J = 7.2 Hz, 6H, $NCH_2C\underline{H}_3$). ^{13}C NMR (126 MHz, $CDCl_3$, 20 °C): δ 166.54 (N$\underline{C}$N−Au), 160.14, 131.79, 119.80, 114.30 (ArC), 130.88 (N$\underline{C}$=$\underline{C}$N), 129.48 (N$\underline{C}$O), 55.27 ($ArO\underline{C}H_3$), 44.27 ($N\underline{C}H_2CH_3$), 16.97 ($NCH_2\underline{C}H_3$). MALDI-TOF/TOF-MS: 533.162 $[M - NCO]^+$, 550.193 $[M - NCO + OH]^+$. Anal. Calcd for $C_{22}H_{24}AuN_2O_3$: C, 45.92; H, 4.20; N, 7.30. Found: C, 45.84; H, 4.10; N, 7.30.

*4.2.12. The Synthesis of Acetate−Gold(I)−NHC Complexes **9** and **10**.* A mixture of silver acetate (40.5 mg, 0.242 mmol) and **1** (57.2 mg, 0.105 mmol) or **2** (60 mg, 0.105 mmol) in CH_2Cl_2 (5 mL) was stirred for 1 h. The mixture was filtered over a bed of Celite, and the filtrate was evaporated to yield a white solid.

*4.2.13. Acetato(1,3-diethyl-4,5-bis(4-fluorophenyl)imidazol-2-ylidene)gold(I) (**9**).* Yield 67%. ^{1}H NMR (500 MHz, $CDCl_3$, 20 °C): δ 7.16 (dd, J = 8.5, 5.3 Hz, 4H, ArH), 7.07 (t, J = 8.5 Hz, 4H, ArH), 4.18 (q, J = 7.2 Hz, 4H, $NC\underline{H}_2CH_3$), 2.09 (s, 3H, $C\underline{H}_3COO$) 1.33 (t, J = 7.2 Hz, 6H, $NCH_2C\underline{H}_3$). ^{13}C NMR (126 MHz, $CDCl_3$, 20 °C): δ 177.47 ($CH_3\underline{C}OO$), 162.85 (N$\underline{C}$N−Au), 164.16, 162.17, 132.41, 132.34, 123.53, 123.50, 116.38, 116.20 (ArC), 130.44 (N$\underline{C}$=$\underline{C}$N), 44.53 ($N\underline{C}H_2CH_3$), 23.85 ($\underline{C}H_3COO$), 16.85 ($N\underline{C}H_2CH_3$). MALDI-TOF/TOF-MS: 509.127 $[M - OAc]^+$,

https://dx.doi.org/10.1021/acs.jmedchem.0c00257
J. Med. Chem. 2020, 63, 9197−9211

526.154 [M − OAc + OH]$^+$. Anal. Calcd for $C_{21}H_{21}AuF_2N_2O_2$: C, 44.38; H, 3.72; N, 4.93. Found: C, 44.47; H, 3.52; N, 4.78.

*4.2.14. Acetato(1,3-diethyl-4,5-bis(4-methoxyphenyl)imidazol-2-ylidene)gold(I) (**10**).* Yield 75%. ^{1}H NMR (500 MHz, $CDCl_3$, 20 °C): δ 7.09 (d, J = 8.7 Hz, 4H, ArH), 6.86 (d, J = 8.7 Hz, 4H, ArH), 4.16 (q, J = 7.2 Hz, 4H, NCH_2CH_3), 3.80 (s, 6H, $ArOCH_3$), 2.09 (s, 3H, CH_3COO), 1.32 (t, J = 7.2 Hz, 6H, NCH_2CH_3). ^{13}C NMR (126 MHz, $CDCl_3$, 20 °C): δ 177.51 (CH_3COO), 161.52(NCN−Au), 160.11, 131.81, 119.93, 114.28 (ArC), 130.89 (NC=CN), 55.26 ($ArOCH_3$), 44.35 (NCH_2CH_3), 23.89 (CH_3COO), 16.89 (NCH_2CH_3). MALDI-TOF/TOF-MS: 533.167 [M − OAc]$^+$, 550.196 [M − OAc + OH]$^+$. Anal. Calcd for $C_{23}H_{27}AuN_2O_4$: C, 46.63; H, 4.59; N, 4.73. Found: C, 46.51; H, 4.52; N, 4.89.

4.3. X-ray Crystallographic Analysis. Single crystal X-ray diffraction data of complex **6** were collected on a Bruker Smart APEX II CCD area-detector diffractometer with graphite-monochromated Mo Kα radiation (0.71073 Å). More detailed data can be obtained free of charge from the Cambridge Crystallographic Data Centre via www.ccdc.cam.ac.uk/structures using CCDC number 1973303 or DOI 10.5517/ccdc.csd.cc247cyq.

4.4. Stability Analysis. *4.4.1. ^{1}H NMR assay.* The NHC−gold(I) complex **6** was dissolved in acetone-d_6 or an acetone-d_6 solution containing 10% D_2O at a concentration of 10 mM. The solutions were transferred to an NMR tube and detected by ^{1}H NMR spectra at different times (0−5 days).

4.4.2. UV−Vis Assay. The stability of **2**, **4**, and **6** (20 μM) in PBS (pH 7.28) with a high concentration of GSH (2 mM) was studied by UV−vis spectrometry via a Shimadzu UV2400 spectrophotometer.

4.5. Growth Inhibitory Assay. All compounds, including cisplatin and auranofin, were dissolved in DMF. They were subsequently diluted to their final assay concentrations (0.1% v/v DMF) before treatment of the cultured cells. HCC (HepG2, SMMC-7721, or Hep3B) cells and noncancerous cells (LO2 and H8) were seeded into 96-well plates (2×10^3 per well). The cells were cultured overnight in DMEM supplemented with 10% FBS. Then, after the addition of different concentrations of compounds and the negative control (0.1% DMF), cells were incubated at 37 °C for 72 h.

The antiproliferative effects of the compounds were tested by the MTT assay by adding 5% MTT (5 mg/mL, PBS) reagent to the cells and incubating the mixture for about 4 h. Then, supernatant was discarded, 200 μL of DMSO was added, and the mixture was shaken for about 10 min. Finally, the absorbance was detected at 490 nm. The XTT assay (cell signaling no. 9095) was performed according to the protocol. In brief, the medium containing XTT and the electron-coupling reagent reacted for 4 h. The absorbance of the wells was determined at 450 nm. The growth inhibitory rates of the compounds were calculated by XTT assays as (Ac − As)/(Ac − Ab) × 100% (Ac, absorbance of control wells; As, absorbance of sample wells; and Ab, Absorbance of blank wells). LDH assays were used to test the cell death as cell death (%) = (As − Ac)/(Am − Ac) × 100 (As, absorbance of sample wells; Ac, absorbance of control wells; and Am, absorbance of the maximum enzyme activity wells). The IC_{50} values corresponding to the concentration that caused 50% of the inhibition of the cell proliferation were calculated using Graphpad Prism 5 statistical analysis.

After incubation with the target compounds under hypoxic conditions (1% O_2, 5% CO_2, and 94% N_2 at 37 °C) for 72 h, cytotoxicity of the cells was measured.

4.6. Purified TrxR Enzyme Assay. TrxR activity was detected by the NADPH-dependent reduction of DTNB at room temperature. Briefly, different concentrations of gold complex **6** were dissolved in DMF and diluted with the respective buffers. Next, 25 μL of rat liver TrxR buffer (0.15 U) and 25 μL of DMF containing the complexes were added into the 96-well plates. Then, to each well was added 225 μL of the reaction mixture. DTNB (20 mM) was added into the solution. After fully mixing, the absorption data was recorded at 405 nm with a microplate reader, and the enzyme activity was calculated as its slope.

4.7. Quantitative Real-Time PCR. According to the protocol, real-time PCR was executed by a 7500 RT-PCR system as described previously.[50] The following primers (GenScript) were used:

- β-actin (forward): 5′-TGTG-GATC-AGCA-AGCA-GGAG-TA-3′,
- β-actin (reverse): 5′-TGCG-CAAG-TTAG-GTTT-TGTCA-3′.
- TrxR (forward): 5′-GCCC-TGCA-AGAC-TCTC-GAAA-TTA-3′,
- TrxR (reverse): 5′-GCCC-ATAA-GCAT-TCTC-ATAG-ACGA-3′.

4.8. Cellular Activities of the TrxR Assay. HepG2 cells were treated with complex **6** and incubated for 48 and 72 h. The total cell protein was extracted in an ice bath and determined from the protein concentration by BCA assays. TrxR activity in the cells was tested by the TrxR activity detection kit.

4.9. Immunofluorescence Staining. The experiments were carried out according to the protocol.[58] In brief, HepG2 cells were treated with complex **6** for 24 h. Different antibodies were incubated overnight at 4 °C. PBS was used to wash the cells, and then they were treated with the secondary antibody for 2 h. Finally, a fluorescence microscope was used to detect the change of fluorescence.

4.10. Western Blot Analysis. HepG2 cell extracts were prepared by washing the cells in cold PBS, followed by resuspension in the cell lysis buffer. Cell lysis buffers were separated by a 12.5% SDS-PAGE gel. After the separation process, the proteins were imprinted onto the PVDF membranes and probed with various specific antibodies. Then, they were washed and incubated with the antirabbit or antimouse for 2 h. The bands of protein were detected by a chemiluminescence procedure (ECL, Amersham).

4.11. Intracellular ROS Measurement. Cells were incubated with complex **6** at different concentrations for 12 h. Then, they were washed and treated in darkness with either 10 μM CM-DCFH2-DA or 20 μM DHE for 20 min at 37 °C. The increase of fluorescence was tested by fluorescent microscopy.

4.12. Measurement of MMP. Cells were seeded in a 24-well plate and then treated with either complex **6** or DMF for 24 h. After that, the cells were treated with JC-1 (5 μM) for 30 min. The cell staining was detected by fluorescence microscopy.

4.13. Cell Cycle Arrest and Apoptosis Analysis. HepG2 cells were treated with either DMF or complex **6** at different concentrations for 72 h. In brief, either DNA flow cytometric kits or annexin V-FITC apoptosis assay kits were used to determine the stage of the cell cycle and apoptosis according to the protocol by flow cytometry.

4.14. Animals. The animal experiments were performed in accordance with the Act on Experimental Work with Animals. All mice were maintained in specific pathogen-free conditions. All mice experiments were performed in compliance with the guidelines and protocols, which were approved by the institutional and local ethics committee of Nanjing University of Chinese Medicine.

4.15. Tumor Nude Mice Model. Male BALB/c nude mice (18−22 g) were inoculated with HepG2 cells (1.5×10^7per mouse). Once the tumor reached 180−200 mm^3, the mice were split into three groups (n = 4) at random. Then, complex **6** (5 mg/kg), cisplatin (5 mg/kg), or the same volume of normal saline intraperitoneally administered for 15 days. Using a digital caliper to gauge the tumor size and calculate the tumor volume (TV), the following formula was used: TV (mm^3) = width^2 × (length/2). The inhibition rates of tumor growth (IRT) were calculated as follows: IRT = 100% × (M_1 − M_2)/M_1, where M_1 and M_2 are the tumor weights in the control group and the drug treatment group, respectively.

4.16. Chronic HCC Model Caused by CCl_4. Four week old male ICR mice (18−22 g) were randomly divided into four groups (n = 5). Group one was the vehicle control, group two was the CCl_4 model group, group three was the complex **6** treatment group, and group four was the positive control group (cisplatin). Groups two through four were intraperitoneally injected with CCl_4 (5 mL/kg) three times every week and treated for 16 weeks to induce HCC. Groups three

https://dx.doi.org/10.1021/acs.jmedchem.0c00257
J. Med. Chem. 2020, 63, 9197−9211

and four were treated with complex **6** (5 mg/kg) and cisplatin (5 mg/kg), respectively, daily for two weeks. After 16 weeks, liver tissues and blood samples were collected, and the liver tissues were fixed in a 4% paraformaldehyde buffer.

4.17. Enzyme-linked Immunosorbent Assay (ELISA). ELISA kits were used to measure the serum levels of TrxR (Nanjing Sen Bei Jia).

4.18. Biochemical Analysis. Serum samples were separated and used for LDH, ALT, and AST tests (Beyotime Biotechnology). The plate reader (PerkinElmer Fusion Reader) was used to measure the absorbance values according to the manufacturer's protocol.

■ ASSOCIATED CONTENT

Supporting Information

The Supporting Information is available free of charge at https://pubs.acs.org/doi/10.1021/acs.jmedchem.0c00257.

Stability information, antiproliferative effects, cell death effects, and additional data and spectra (PDF)

Molecular formula strings and biological data (CSV)

■ AUTHOR INFORMATION

Corresponding Author

Wukun Liu − *Jiangsu Collaborative Innovation Center of Chinese Medicinal Resources Industrialization, School of Pharmacy, School of Medicine & Holistic Integrative Medicine, Nanjing University of Chinese Medicine, Nanjing 210023, P. R. China; State Key Laboratory of Natural Medicines, China Pharmaceutical University, Nanjing 210009, P. R. China; State Key Laboratory of Coordination Chemistry, Nanjing University, Nanjing 210023, P. R. China;* orcid.org/0000-0002-0469-907X; Phone: +86-25-85811633; Email: liuwukun0000@hotmail.com, liuwukun0000@njucm.edu.cn

Authors

Mianli Bian − *Jiangsu Collaborative Innovation Center of Chinese Medicinal Resources Industrialization, School of Pharmacy, School of Medicine & Holistic Integrative Medicine, Nanjing University of Chinese Medicine, Nanjing 210023, P. R. China*

Rong Fan − *Jiangsu Collaborative Innovation Center of Chinese Medicinal Resources Industrialization, School of Pharmacy, School of Medicine & Holistic Integrative Medicine, Nanjing University of Chinese Medicine, Nanjing 210023, P. R. China*

Guizhi Jiang − *Jiangsu Collaborative Innovation Center of Chinese Medicinal Resources Industrialization, School of Pharmacy, School of Medicine & Holistic Integrative Medicine, Nanjing University of Chinese Medicine, Nanjing 210023, P. R. China*

Yingxiang Wang − *Jiangsu Collaborative Innovation Center of Chinese Medicinal Resources Industrialization, School of Pharmacy, School of Medicine & Holistic Integrative Medicine, Nanjing University of Chinese Medicine, Nanjing 210023, P. R. China*

Yunlong Lu − *Jiangsu Collaborative Innovation Center of Chinese Medicinal Resources Industrialization, School of Pharmacy, School of Medicine & Holistic Integrative Medicine, Nanjing University of Chinese Medicine, Nanjing 210023, P. R. China*

Complete contact information is available at: https://pubs.acs.org/10.1021/acs.jmedchem.0c00257

Author Contributions

[||]M.B. and R.F. contributed equally to this work.

Notes

The authors declare no competing financial interest.

■ ACKNOWLEDGMENTS

The authors thank the financial support from the National Natural Science Foundation of China (NSFC) (Grant 81703337); the Priority Academic Program Development of Jiangsu Higher Education Institutions (Integration of Chinese and Western Medicine); the Jiangsu Specially-Appointed Professors program; the Six Talent Peaks Project in the Jiangsu Province of China (Grant SWYY-069); the State Key Laboratory of Coordination Chemistry; Nanjing University; and the Open Project of State Key Laboratory of Natural Medicines, China Pharmaceutical University (Grants SKLNMKF201712 and SKLNMKF201808).

■ ABBREVIATIONS USED

ALT, alanine aminotransferase; AST, aspartate aminotransferase; CCl_4, carbon tetrachloride; CDKs, cyclin dependent protein kinase; CT-DNA, calf thymus DNA; DHE, dihydroethidium; IRT, rate of tumor growth; HCC, hepatocellular carcinoma; LDH, lactate dehydrogenase; IL-1β, Interleukin-1β; MMP, mitochondrial membrane potential; NAC, *N*-acetylcysteine; PBS, phosphate buffer solution; ROS, reactive oxygen species; TNF-α, tumor necrosis factor; TrxR, thioredoxin reductase

■ REFERENCES

(1) Jiang, Y.; Sun, A.; Zhao, Y.; Ying, W.; Sun, H.; Yang, X.; Xing, B.; Sun, W.; Ren, L.; Hu, B.; Li, C.; Zhang, L.; Qin, G.; Zhang, M.; Chen, N.; Zhang, M.; Huang, Y.; Zhou, J.; Zhao, Y.; Liu, M.; Zhu, X.; Qiu, Y.; Sun, Y.; Huang, C.; Yan, M.; Wang, M.; Liu, W.; Tian, F.; Xu, H.; Zhou, J.; Wu, Z.; Shi, T.; Zhu, W.; Qin, J.; Xie, L.; Fan, J.; Qian, X.; He, F. Proteomics identifies new therapeutic targets of early-stage hepatocellular carcinoma. *Nature* **2019**, *567*, 257−261.

(2) Siegel, R.; Naishadham, D.; Jemal, A. Cancer statistics, 2013. *Ca-Cancer J. Clin.* **2013**, *63*, 11−30.

(3) Feng, R. M.; Zong, Y. N.; Cao, S. M.; Xu, R. H. Current cancer situation in China: good or bad news from the 2018 global cancer statistics? *Cancer Commun. (Lond)* **2019**, *39*, 22.

(4) Mancarella, S.; Krol, S.; Crovace, A.; Leporatti, S.; Dituri, F.; Frusciante, M.; Giannelli, G. Validation of hepatocellular carcinoma experimental models for TGF-beta promoting tumor progression. *Cancers* **2019**, *11*, 1510.

(5) Casini, A.; Wai-Yin Sun, R.; Ott, I. Medicinal chemistry of gold anticancer metallodrugs. *Met. Ions. Life. Sci.* **2018**, *18*, 199−217.

(6) Nobili, S.; Mini, E.; Landini, I.; Gabbiani, C.; Casini, A.; Messori, L. Gold compounds as anticancer agents: chemistry, cellular pharmacology, and preclinical studies. *Med. Res. Rev.* **2010**, *30*, 550−580.

(7) Zou, T.; Lum, C. T.; Lok, C. N.; Zhang, J. J.; Che, C. M. Chemical biology of anticancer gold(III) and gold(I) complexes. *Chem. Soc. Rev.* **2015**, *44*, 8786−8801.

(8) Berners-Price, S. J.; Filipovska, A. Gold compounds as therapeutic agents for human diseases. *Metallomics* **2011**, *3*, 863−873.

(9) Bertrand, B.; Casini, A. A golden future in medicinal inorganic chemistry: the promise of anticancer gold organometallic compounds. *Dalton Trans.* **2014**, *43*, 4209−4219.

(10) Zhang, X.; Selvaraju, K.; Saei, A. A.; D'Arcy, P.; Zubarev, R. A.; Arner, E. S.; Linder, S. Repurposing of auranofin: thioredoxin reductase remains a primary target of the drug. *Biochimie* **2019**, *162*, 46−54.

(11) Marzo, T.; Massai, L.; Pratesi, A.; Stefanini, M.; Cirri, D.; Magherini, F.; Becatti, M.; Landini, I.; Nobili, S.; Mini, E.; Crociani, O.; Arcangeli, A.; Pillozzi, S.; Gamberi, T.; Messori, L. Replacement of the thiosugar of auranofin with iodide enhances the anticancer

potency in a mouse model of ovarian cancer. *ACS Med. Chem. Lett.* **2019**, *10*, 656−660.
(12) Sze, J. H.; Raninga, P. V.; Nakamura, K.; Casey, M.; Khanna, K. K.; Berners-Price, S. J.; Di Trapani, G.; Tonissen, K. F. Anticancer activity of a Gold(I) phosphine thioredoxin reductase inhibitor in multiple myeloma. *Redox Biol.* **2020**, *28*, 101310.
(13) Lee, D.; Xu, I. M. J.; Chiu, D. K. C.; Leibold, J.; Tse, A. P. W.; Bao, M. H. R.; Yuen, V. W. H.; Chan, C. Y. K.; Lai, R. K. H.; Chin, D. W. C.; Chan, D. F. F.; Cheung, T. T.; Chok, S. H.; Wong, C. M.; Lowe, S. W.; Ng, I. O. L.; Wong, C. C. L. Induction of oxidative stress through inhibition of thioredoxin reductase 1 is an effective therapeutic approach for hepatocellular carcinoma. *Hepatology* **2019**, *69*, 1768−1786.
(14) Rackham, O.; Shearwood, A. M.; Thyer, R.; McNamara, E.; Davies, S. M.; Callus, B. A.; Miranda-Vizuete, A.; Berners-Price, S. J.; Cheng, Q.; Arner, E. S.; Filipovska, A. Substrate and inhibitor specificities differ between human cytosolic and mitochondrial thioredoxin reductases: implications for development of specific inhibitors. *Free Radical Biol. Med.* **2011**, *50*, 689−699.
(15) Li, C.; Peng, Y.; Mao, B.; Qian, K. Thioredoxin reductase: a novel, independent prognostic marker in patients with hepatocellular carcinoma. *Oncotarget* **2015**, *6*, 17792−17804.
(16) Zheng, X.; Ma, W.; Sun, R.; Yin, H.; Lin, F.; Liu, Y.; Xu, W.; Zeng, H. Butaselen prevents hepatocarcinogenesis and progression through inhibiting thioredoxin reductase activity. *Redox Biol.* **2018**, *14*, 237−249.
(17) Zhang, L.; Cheng, Q.; Zhang, L.; Wang, Y.; Merrill, G. F.; Ilani, T.; Fass, D.; Arnér, E. S. J.; Zhang, J. Serum thioredoxin reductase is highly increased in mice with hepatocellular carcinoma and its activity is restrained by several mechanisms. *Free Radical Biol. Med.* **2016**, *99*, 426−435.
(18) Bertrand, B.; Williams, M. R. M.; Bochmann, M. Gold(III) complexes for antitumor applications: an overview. *Chem. - Eur. J.* **2018**, *24*, 11840−11851.
(19) Gust, R.; Ott, I.; Posselt, D.; Sommer, K. Development of cobalt(3,4-diarylsalen) complexes as tumor therapeutics. *J. Med. Chem.* **2004**, *47*, 5837−5846.
(20) Ott, I. On the medicinal chemistry of gold complexes as anticancer drugs. *Coord. Chem. Rev.* **2009**, *253*, 1670−1681.
(21) Schmidt, C.; Karge, B.; Misgeld, R.; Prokop, A.; Bronstrup, M.; Ott, I. Biscarbene gold(i) complexes: structure-activity-relationships regarding antibacterial effects, cytotoxicity, TrxR inhibition and cellular bioavailability. *MedChemComm* **2017**, *8*, 1681−1689.
(22) Liu, W.; Bensdorf, K.; Proetto, M.; Abram, U.; Hagenbach, A.; Gust, R. NHC gold halide complexes derived from 4,5-diarylimidazoles: synthesis, structural analysis, and pharmacological investigations as potential antitumor agents. *J. Med. Chem.* **2011**, *54*, 8605−8615.
(23) Liu, W.; Bensdorf, K.; Hagenbach, A.; Abram, U.; Niu, B.; Mariappan, A.; Gust, R. Synthesis and biological studies of silver N-heterocyclic carbene complexes derived from 4,5-diarylimidazole. *Eur. J. Med. Chem.* **2011**, *46*, 5927−5934.
(24) Meyer, A.; Oehninger, L.; Geldmacher, Y.; Alborzinia, H.; Wolfl, S.; Sheldrick, W. S.; Ott, I. Gold(I) N-heterocyclic carbene complexes with naphthalimide ligands as combined thioredoxin reductase inhibitors and DNA intercalators. *ChemMedChem* **2014**, *9*, 1794−1800.
(25) Zou, T.; Lum, C. T.; Chui, S. S.; Che, C. M. Gold(III) complexes containing N-heterocyclic carbene ligands: thiol "switch-on" fluorescent probes and anti-cancer agents. *Angew. Chem., Int. Ed.* **2013**, *52*, 2930−2933.
(26) Ott, I. Metal N-heterocyclic carbene complexes in medicinal chemistry. *Adv. Inorg. Chem.* **2020**, *75*, 121−148.
(27) Liu, W.; Gust, R. Metal N-heterocyclic carbene complexes as potential antitumor metallodrugs. *Chem. Soc. Rev.* **2013**, *42*, 755−773.
(28) Hickey, J. L.; Ruhayel, R. A.; Barnard, P. J.; Baker, M. V.; Berners-Price, S. J.; Filipovska, A. Mitochondria-targeted chemotherapeutics: the rational design of gold(I) N-heterocyclic carbene complexes that are selectively toxic to cancer cells and target protein selenols in preference to thiols. *J. Am. Chem. Soc.* **2008**, *130*, 12570−12571.
(29) Liu, W.; Gust, R. Update on metal N-heterocyclic carbene complexes as potential anti-tumor metallodrugs. *Coord. Chem. Rev.* **2016**, *329*, 191−213.
(30) Schmidt, C.; Albrecht, L.; Balasupramaniam, S.; Misgeld, R.; Karge, B.; Bronstrup, M.; Prokop, A.; Baumann, K.; Reichl, S.; Ott, I. A gold(I) biscarbene complex with improved activity as a TrxR inhibitor and cytotoxic drug: comparative studies with different gold metallodrugs. *Metallomics* **2019**, *11*, 533−545.
(31) Baker, M. V.; Barnard, P. J.; Brayshaw, S. K.; Hickey, J. L.; Skelton, B. W.; White, A. H. Synthetic, structural and spectroscopic studies of (pseudo)halo(1,3-di-tert-butylimidazol-2-ylidine)gold complexes. *Dalton Trans.* **2005**, *1*, 37−43.
(32) Messori, L.; Marchetti, L.; Massai, L.; Scaletti, F.; Guerri, A.; Landini, I.; Nobili, S.; Perrone, G.; Mini, E.; Leoni, P.; Pasquali, M.; Gabbiani, C. Chemistry and biology of two novel gold(I) carbene complexes as prospective anticancer agents. *Inorg. Chem.* **2014**, *53*, 2396−2403.
(33) Marzo, T.; Cirri, D.; Gabbiani, C.; Gamberi, T.; Magherini, F.; Pratesi, A.; Guerri, A.; Biver, T.; Binacchi, F.; Stefanini, M.; Arcangeli, A.; Messori, L. Auranofin, Et3PAuCl, and Et3PAuI are highly cytotoxic on colorectal cancer cells: a chemical and biological study. *ACS Med. Chem. Lett.* **2017**, *8*, 997−1001.
(34) Karaca, O.; Scalcon, V.; Meier-Menches, S. M.; Bonsignore, R.; Brouwer, J.; Tonolo, F.; Folda, A.; Rigobello, M. P.; Kuhn, F. E.; Casini, A. Characterization of hydrophilic gold(I) N-heterocyclic carbene (NHC) complexes as potent TrxR inhibitors using biochemical and mass spectrometric approaches. *Inorg. Chem.* **2017**, *56*, 14237−14250.
(35) Mirzayans, R.; Andrais, B.; Murray, D. Do Multiwell Plate High Throughput Assays Measure Loss of Cell Viability Following Exposure to Genotoxic Agents? *Int. J. Mol. Sci.* **2017**, *18*, 1679.
(36) Monteiro-Riviere, N. A.; Inman, A. O.; Zhang, L. W. Limitations and relative utility of screening assays to assess engineered nanoparticle toxicity in a human cell line. *Toxicol. Appl. Pharmacol.* **2009**, *234*, 222−235.
(37) Ott, I.; Qian, X.; Xu, Y.; Vlecken, D. H.; Marques, I. J.; Kubutat, D.; Will, J.; Sheldrick, W. S.; Jesse, P.; Prokop, A.; Bagowski, C. P. A gold(I) phosphine complex containing a naphthalimide ligand functions as a TrxR inhibiting antiproliferative agent and angiogenesis inhibitor. *J. Med. Chem.* **2009**, *52*, 763−770.
(38) Bian, M.; Fan, R.; Zhao, S.; Liu, W. Targeting the thioredoxin system as a strategy for cancer therapy. *J. Med. Chem.* **2019**, *62*, 7309−7321.
(39) Zhang, J.; Zhang, B.; Li, X.; Han, X.; Liu, R.; Fang, J. Small molecule inhibitors of mammalian thioredoxin reductase as potential anticancer agents: an update. *Med. Res. Rev.* **2019**, *39*, 5−39.
(40) Zhang, B.; Liu, Y.; Li, X.; Xu, J.; Fang, J. Small molecules to target the selenoprotein thioredoxin reductase. *Chem. - Asian J.* **2018**, *13*, 3593−3600.
(41) Huang, K. B.; Wang, F. Y.; Tang, X. M.; Feng, H. W.; Chen, Z. F.; Liu, Y. C.; Liu, Y. N.; Liang, H. Organometallic gold(III) complexes similar to tetrahydroisoquinoline induce ER-stress-mediated apoptosis and pro-death autophagy in A549 cancer cells. *J. Med. Chem.* **2018**, *61*, 3478−3490.
(42) Bian, M.; Sun, Y.; Liu, Y.; Xu, Z.; Fan, R.; Liu, Z.; Liu, W. A gold(I) complex containing an oleanolic acid derivative as a potential anti-ovarian cancer agent via inhibiting TrxR and activating ROS-mediated ERS. *Chem. - Eur. J.* **2020**, *26*, 7092−7108.
(43) Wang, K.; Zhu, C.; He, Y.; Zhang, Z.; Zhou, W.; Muhammad, N.; Guo, Y.; Wang, X.; Guo, Z. Restraining cancer cells by dual metabolic inhibition with a mitochondrion-targeted platinum(II) complex. *Angew. Chem., Int. Ed.* **2019**, *58*, 4638−4643.
(44) Kalyanaraman, B.; Darley-Usmar, V.; Davies, K. J.; Dennery, P. A.; Forman, H. J.; Grisham, M. B.; Mann, G. E.; Moore, K.; Roberts, L. J., 2nd; Ischiropoulos, H. Measuring reactive oxygen and nitrogen species with fluorescent probes: challenges and limitations. *Free Radical Biol. Med.* **2012**, *52*, 1−6.

https://dx.doi.org/10.1021/acs.jmedchem.0c00257
J. Med. Chem. 2020, 63, 9197−9211

(45) Wu, K. J.; Zhong, H. J.; Yang, G.; Wu, C.; Huang, J. M.; Li, G.; Ma, D. L.; Leung, C. H. Small molecule Pin1 inhibitor blocking NF-kappaB signaling in prostate cancer cells. *Chem. - Asian J.* **2018**, *13*, 275−279.
(46) Wu, K. J.; Zhong, H. J.; Li, G.; Liu, C.; Wang, H. D.; Ma, D. L.; Leung, C. H. Structure-based identification of a NEDD8-activating enzyme inhibitor via drug repurposing. *Eur. J. Med. Chem.* **2018**, *143*, 1021−1027.
(47) Nishanth, R. P.; Jyotsna, R. G.; Schlager, J. J.; Hussain, S. M.; Reddanna, P. Inflammatory responses of RAW 264.7 macrophages upon exposure to nanoparticles: role of ROS-NFkappaB signaling pathway. *Nanotoxicology* **2011**, *5*, 502−516.
(48) Hsu, C. C.; Lien, J. C.; Chang, C. W.; Chang, C. H.; Kuo, S. C.; Huang, T. F. Yuwen02f1 suppresses LPS-induced endotoxemia and adjuvant-induced arthritis primarily through blockade of ROS formation, NFkB and MAPK activation. *Biochem. Pharmacol.* **2013**, *85*, 385−395.
(49) Huang, Q.; Zhan, L.; Cao, H.; Li, J.; Lyu, Y.; Guo, X.; Zhang, J.; Ji, L.; Ren, T.; An, J.; Liu, B.; Nie, Y.; Xing, J. Increased mitochondrial fission promotes autophagy and hepatocellular carcinoma cell survival through the ROS-modulated coordinated regulation of the NFKB and TP53 pathways. *Autophagy* **2016**, *12*, 999−1014.
(50) Fan, R.; Bian, M.; Hu, L.; Liu, W. A new rhodium(I) NHC complex inhibits TrxR: In vitro cytotoxicity and in vivo hepatocellular carcinoma suppression. *Eur. J. Med. Chem.* **2019**, *183*, 111721.
(51) Huang, W.; Liu, Y.; Wang, J.; Yuan, X.; Jin, H. W.; Zhang, L. R.; Zhang, J. T.; Liu, Z. M.; Cui, J. R. Small-molecule compounds targeting the STAT3 DNA-binding domain suppress survival of cisplatin-resistant human ovarian cancer cells by inducing apoptosis. *Eur. J. Med. Chem.* **2018**, *157*, 887−897.
(52) Bian, M.; Chen, X.; Zhang, C.; Jin, H.; Wang, F.; Shao, J.; Chen, A.; Zhang, F.; Zheng, S. Magnesium isoglycyrrhizinate promotes the activated hepatic stellate cells apoptosis via endoplasmic reticulum stress and ameliorates fibrogenesis in vitro and in vivo. *Biofactors* **2017**, *43*, 836−846.
(53) Raoof, M.; Corr, S. J.; Zhu, C.; Cisneros, B. T.; Kaluarachchi, W. D.; Phounsavath, S.; Wilson, L. J.; Curley, S. A. Gold nanoparticles and radiofrequency in experimental models for hepatocellular carcinoma. *Nanomedicine* **2014**, *10*, 1121−1130.
(54) Newell, P.; Villanueva, A.; Friedman, S. L.; Koike, K.; Llovet, J. M. Experimental models of hepatocellular carcinoma. *J. Hepatol.* **2008**, *48*, 858−879.
(55) Reyes-Gordillo, K.; Shah, R.; Arellanes-Robledo, J.; Cheng, Y.; Ibrahim, J.; Tuma, P. L. Akt1 and Akt2 isoforms play distinct roles in regulating the development of inflammation and fibrosis associated with alcoholic liver disease. *Cells* **2019**, *8*, 1337.
(56) Pawlak, M.; Lefebvre, P.; Staels, B. Molecular mechanism of PPARalpha action and its impact on lipid metabolism, inflammation and fibrosis in non-alcoholic fatty liver disease. *J. Hepatol.* **2015**, *62*, 720−733.
(57) Zhou, H.; Yu, M.; Zhao, J.; Martin, B. N.; Roychowdhury, S.; McMullen, M. R.; Wang, E.; Fox, P. L.; Yamasaki, S.; Nagy, L. E.; Li, X. IRAKM-Mincle axis links cell death to inflammation: Pathophysiological implications for chronic alcoholic liver disease. *Hepatology* **2016**, *64*, 1978−1993.
(58) Bian, M.; He, J.; Jin, H.; Lian, N.; Shao, J.; Guo, Q.; Wang, S.; Zhang, F.; Zheng, S. Oroxylin A induces apoptosis of activated hepatic stellate cells through endoplasmic reticulum stress. *Apoptosis* **2019**, *24*, 905−920.

https://dx.doi.org/10.1021/acs.jmedchem.0c00257
J. Med. Chem. 2020, 63, 9197−9211